

Deep-subwavelength interface states in mechanical systems



Guobiao Hu ^a, Chunbo Lan ^b, Lihua Tang ^c, Yaowen Yang ^{a,*}

^a School of Civil and Environmental Engineering, Nanyang Technological University, 50 Nanyang Avenue, 639798, Singapore

^b College of Aerospace Engineering, Nanjing University of Aeronautics and Astronautics, Nanjing, Jiangsu 210016, China

^c Department of Mechanical Engineering, University of Auckland, 20 Symonds Street, Auckland 1010, New Zealand

ARTICLE INFO

Keywords:

Mass-spring systems
Rod and beam
Interface states
Deep-subwavelength
Quasi-static band gap

ABSTRACT

Topological interface states in mechanical systems are the analogues of the edge modes in topological insulators from the field of condensed matter physics. The interface states produced and reported in the existing literature are located in the Bragg Scattering band gaps of phononic crystals. The corresponding frequencies of the interface states are thus high. This paper proposes a novel mechanical system that can produce an ultra-low frequency interface state in the deep-subwavelength region. Due to the periodic spring connections to the ground, a quasi-static band gap with a starting frequency of 0 Hz can be produced in the proposed system. The spring connections can be tuned to alter the polarization direction of the mode shape. Through a mass-spring model, the formation of an interface state in the quasi-static band gap is demonstrated. Moreover, it is found that by carefully configuring the spring connections to the ground, the interface state in the quasi-static band gap can be tuned to an arbitrarily low frequency. In addition, practical systems based on rod and beam structures are constructed following a similar design methodology. Theoretical analyses demonstrate that for the longitudinal/transverse wave mode in the topological rod/beam structure, a deep-subwavelength interface state can always form in the quasi-static band gap. The possibility of producing the deep-subwavelength interface state at an arbitrarily low frequency is also confirmed in a rod and a beam lattice system.

1. Introduction

In recent years, extensive research interests have been attracted by topological insulators [1–3] from the field of condensed matter physics. The bulk-edge correspondence and the topologically protected edge modes are the most interesting properties of topological insulators. Inspired by these discoveries in quantum physics, tremendous efforts have been devoted to developing mechanical analogues of topological insulators and exploring topological states in classical mechanics [4–15]. According to the literature review, topological acoustic/mechanical systems are often developed using sonic/phononic crystals based on their excellent wave manipulation capabilities. Topological interface states can be produced in the Bragg Scattering (BS) band gaps of carefully engineered phononic crystals. In the acoustic domain, based on the typical Su-Schrieffer-Heeger (SSH) model [16], Yang *et al.* [17] developed an acoustic analogue and demonstrated the formation of a topological interface state in the BS band gap of the acoustic system. Xiao *et al.* [18] prototyped an acoustic topological system and observed the interface state in the experimental study. In the mechanical domain, Pal *et al.* [19] implemented the topological concept in the design of an elastic plate. By an intentional design of two halves of the plate with different topological invariants, an edge wave of the frequency within the bulk band gap could propagate along the topological

* Corresponding author.

E-mail address: cwyang@ntu.edu.sg (Y. Yang).

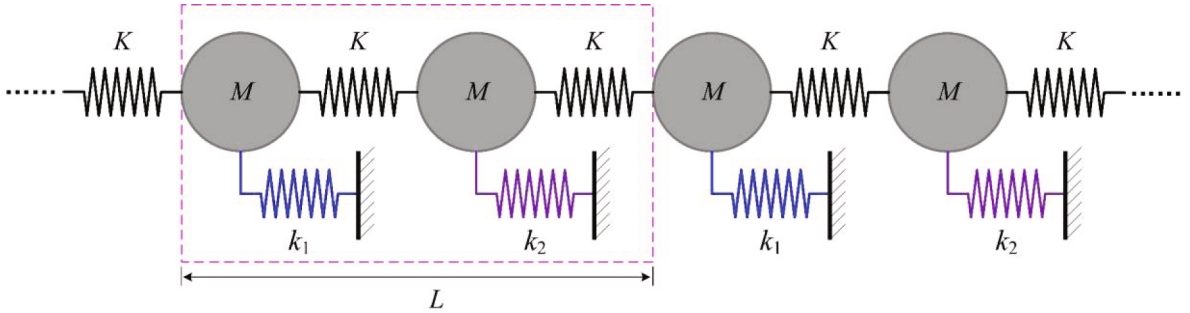


Fig. 1. Schematic of the mass-spring chain with grounded springs.

interface. Muhammad *et al.* [20] designed a one-dimensional topological phononic crystal and theoretically investigated its longitudinal/transverse wave propagation. The interface states were predicted and identified through various means.

Since the interface states reported in the aforementioned literature were formed in the BS band gaps, the corresponding frequencies of the interface states were high. For example, the interface mode of the proposed topological phononic crystal in [20] was 50.5 kHz, and the interface state of the topological system reported in [21] was formed at the frequency of 33.1 kHz. Instead of phononic crystals, Zhao *et al.* [22] explored the interface states in locally resonant metamaterials. Though they found that the interface states could never appear in locally resonant (LR) band gaps, the first BS band gap was produced below the LR band gap, and the frequency of the interface state formed in the first BS band gap was significantly decreased. More recently, Fan *et al.* [23] established a practical acoustic structure based on the idea in [22] and demonstrated the interface state through finite element simulation. To the best of the authors' knowledge, there have been limited studies on producing low-frequency interface states in topological mechanical systems, which is of practical importance in applications such as vibration control, noise reduction and energy harvesting. In retrospect to the fundamental research of metamaterials, we can find a number of metamaterial models that can produce quasi-static band gaps (i.e., the band gap starts from 0 Hz) in the literature. For example, Lee *et al.* [24] experimentally found that an acoustic metamaterial tube with an array of side holes could generate a band gap for forbidding the propagation of sound waves below 450 Hz. Oh *et al.* [25] proposed a metamaterial with subtle joint connections between neighbouring cells. A quasi-static band gap was produced due to the zero rotational stiffness of the proposed metamaterial. Hu *et al.* [26] introduced negative stiffness springs into the design of metamaterials and achieved quasi-static band gaps. Yu *et al.* [27] studied the dynamics of beams with periodic connections to the ground. It was proved that the connections to the ground introduced quasi-static band gaps in the investigated systems. Since ultra-low frequency band gaps can be produced, a question that naturally arises is: could interface states form in the quasi-static band gap?

To answer the above question, a novel approach of producing arbitrarily low-frequency interface states in topological mechanical systems is explored in this paper. First, we present a means of producing quasi-static band gaps in periodic mechanical systems through the introduction of a series of spring connections to the ground. Subsequently, negative stiffness springs are alternatively used to alter the polarization directions of the mode shapes. Finally, supercell band structure and transmittance results are presented to demonstrate the formation of the interface states in the designed system. The effect of the negative stiffness on the interface state formation is discussed in detail. The rest of the work is organized as follows. In Section 2, the proposed design approach is introduced based on a mass-spring model. Practical structures designed by following the proposed approach are presented in Section 3. A rod system for longitudinal waveguiding and a beam system for transverse waveguiding are investigated. Conclusions are summarized in Section 4.

2. Mass-spring model

To demonstrate the approach of producing arbitrarily low-frequency interface states, a mass-spring chain is first considered, as shown in Fig. 1. The host chain consists of particles with uniform mass (M) that are successively linked by springs with identical constant (K). All the particles are connected to the ground through springs with constant k_1 or k_2 . The governing equations of the two particles in a unit cell (marked in the dashed frame) can be written as:

$$\begin{cases} M\ddot{y}_i + K(y_i - y_{j-1}) + K(y_i - y_j) + k_1 y_i = 0 \\ M\ddot{y}_j + K(y_j - y_i) + K(y_j - y_{i+1}) + k_2 y_j = 0 \end{cases} \quad (1)$$

where y represents the displacement of the particle. The subscripts i and j indicate the left-hand side (LHS) and the right-hand side (RHS) particles in the unit cell, respectively. \ddot{y} denotes the second derivative of y with respect to time. To generalize the study presented in the work, the following dimensionless parameters are introduced:

$$\begin{cases} \alpha_1 = \frac{k_1}{K} & \alpha_2 = \frac{k_2}{K} & \Omega_r = \frac{\omega}{\omega_r} \\ \tilde{y}_i = \frac{y_i}{L} & \tilde{y}_j = \frac{y_j}{L} & \tilde{t} = \omega_r t \end{cases} \quad (2)$$

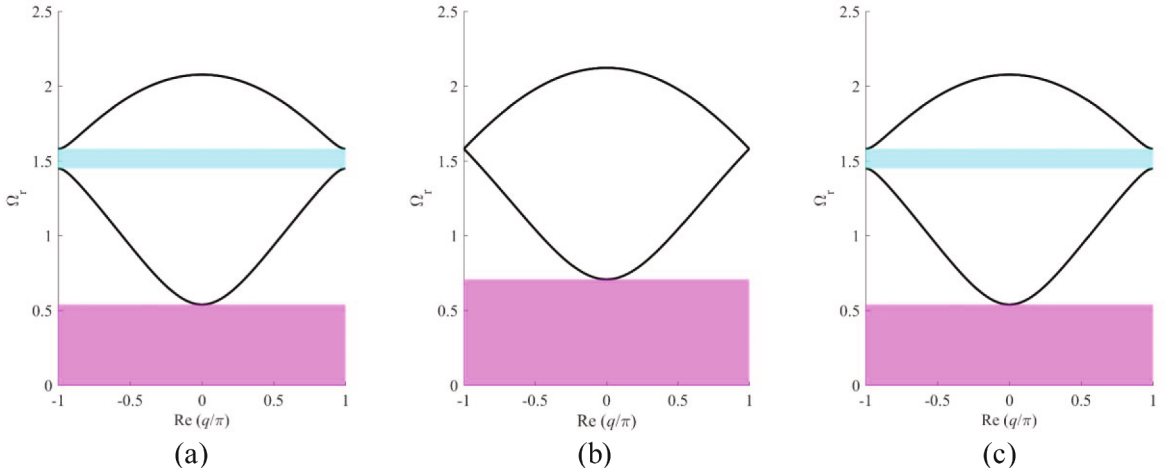


Fig. 2. Band structure of the mass-spring chain for (a) $\alpha_1 = 0.1$ and $\alpha_2 = 0.5$; (b) $\alpha_1 = 0.5$ and $\alpha_2 = 0.5$; (c) $\alpha_1 = 0.5$ and $\alpha_2 = 0.1$.

where $\omega_r = \sqrt{K/M}$, ω is the angular frequency of the wave that propagates in the mass-spring lattice system, and L is the lattice constant, i.e., the unit cell length. By non-dimensionlizing Eq. (1) then applying the Fourier's transform, one obtains:

$$\begin{cases} -\Omega_r^2 Y_i + (2Y_i - Y_{i-1} - Y_j) + \alpha_1 Y_i = 0 \\ -\Omega_r^2 Y_j + (2Y_j - Y_i - Y_{j+1}) + \alpha_2 Y_j = 0 \end{cases} \quad (3)$$

where Y is the dimensionless amplitude of \tilde{y} . We assume the mass-spring chain to have an infinite number of particles. Applying the Bloch's theorem to describe the periodicity yields:

$$\begin{cases} Y_i = e^{iq} Y_{i-1} \\ Y_j = e^{iq} Y_{j-1} \end{cases} \quad (4)$$

where $I = \sqrt{-1}$, and q is the wavenumber normalized with respect to the lattice constant. Substituting Eq. (4) into Eq. (3) gives:

$$\begin{cases} (2 + \alpha_1 - \Omega_r^2) Y_i - (1 + e^{-iq}) Y_j = 0 \\ -(1 + e^{iq}) Y_i + (2 + \alpha_2 - \Omega_r^2) Y_j = 0 \end{cases} \quad (5)$$

To ensure the existence of non-trivial solutions, forcing the determinant of the coefficient matrix of Eq. (5) to be zero yields the dispersion relation for the elastic wave propagating in the mass-spring chain.

$$\Omega_r^4 - (\alpha_1 + \alpha_2 + 4)\Omega_r^2 + \alpha_1\alpha_2 + 2(\alpha_1 + \alpha_2) + 2(1 - \cos(q)) = 0 \quad (6)$$

For different combinations of α_1 and α_2 , Fig. 2 presents the band structures of the corresponding mass-spring chains. It can be seen that when $\alpha_1 = 0.1$ & $\alpha_2 = 0.5$ and $\alpha_1 = 0.5$ & $\alpha_2 = 0.1$, the band structures are exactly the same, and two band gaps are observed. The second band gap in the high-frequency regime is closed when $\alpha_1 = \alpha_2$ and opened when $\alpha_1 \neq \alpha_2$. Thus, it is easy to know that the second band gap is formed due to the Bragg Scattering mechanism [22]. The first band gap is formed by the local resonance mechanism. The proof and the discussion about the formation mechanism are provided in Appendix I.

Investigating the band topology by calculating the Zak phase can predict the existence of topological interface states [28–29]. To be more specific, whether a band gap supports the formation of topological interface states can be predicted by considering the cumulative effect of the topological properties of all the bands below the band gap [22]. However, because of the specialty of the system, no band exists below the first band gap. Another criterion of determining the existence of topological interface states is to check the eigenstate polarization at the band-edge points. The switching of the eigenstate polarization is the symptomatic of the existence of topological interface states. From Eq. (5), the amplitude ratio of the eigenstate on the acoustic band can be obtained as:

$$\frac{Y_i}{Y_j} = \frac{(1 + e^{-iq})}{(2 + \alpha_1 - \Omega_{acoustic}^2)} = \frac{(1 + e^{-iq})/2}{\left(1 + \frac{(\alpha_1 - \alpha_2 - 4) + \sqrt{(\alpha_1 - \alpha_2)^2 + 8(1 + \cos(q))}}{4}\right)} \quad (7)$$

Note that the lower edge of the first band occurs at $q = 0$. Substituting it into Eq. (7) gives:

Table 1
Eigenstate properties at the band-edge points.

		$\alpha_{12} < 0$	$\alpha_{12} > 0$
1st Band gap	Static	$Y_i = Y_j = 0$	$Y_i = Y_j = 0$
	S_1	$Y_i/Y_j > 1$	$Y_i/Y_j < 1$
2nd Band gap	S_2	$Y_i/Y_j \rightarrow \infty$	$Y_i/Y_j \rightarrow 0$
	S_3	$Y_i/Y_j \rightarrow 0$	$Y_i/Y_j \rightarrow \infty$

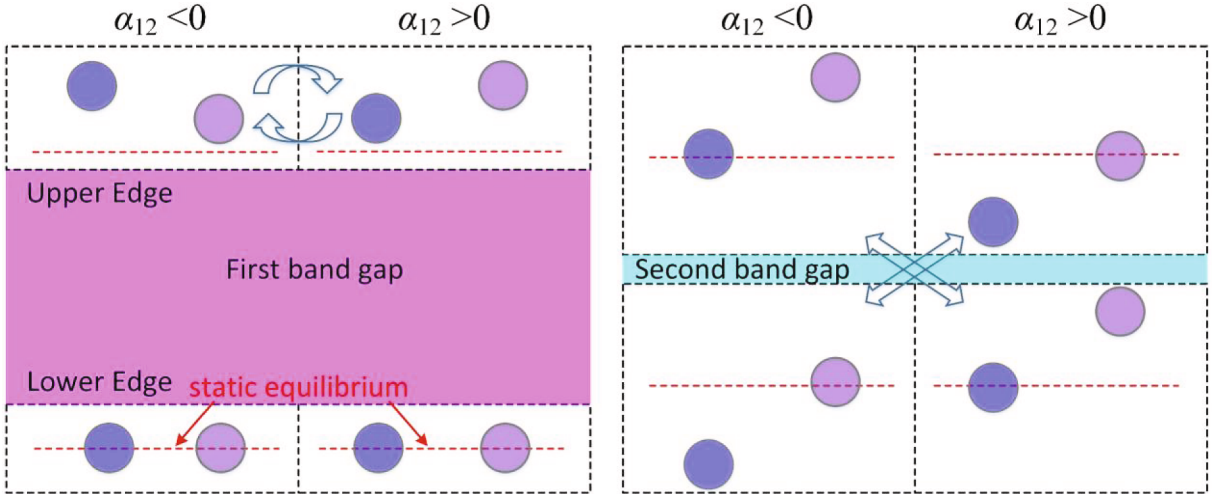


Fig. 3. Graphical demonstration of the eigenstates at the band-edge points.

$$\frac{Y_i}{Y_j} = \frac{(1 + e^{-Iq})}{(2 + \alpha_1 - \Omega_r^2)} \Big|_{q=0} = \frac{1}{\left(1 + \frac{(\alpha_{12}-4)+\sqrt{\alpha_{12}^2+16}}{4}\right)} \quad (8)$$

where $\alpha_{12} = \alpha_1 - \alpha_2$. It is easy to prove that:

$$\begin{cases} \alpha_{12} > 0 & Y_i/Y_j < 1 \\ \alpha_{12} < 0 & Y_i/Y_j > 1 \end{cases} \quad (9)$$

Therefore, one knows that if $\alpha_1 \neq \alpha_2$, swapping α_1 and α_2 will lead to a different amplitude ratio of the eigenstate at the edge point just above the first band gap. Similarly, the amplitude ratio of the eigenstate on the optical band can be obtained as:

$$\frac{Y_i}{Y_j} = \frac{(1 + e^{-Iq})}{(2 + \alpha_1 - \Omega_{optical}^2)} = \frac{(1 + e^{-Iq})/2}{\left(1 + \frac{(\alpha_1-\alpha_2-4)-\sqrt{(\alpha_1-\alpha_2)^2+8(1+\cos(q))}}{4}\right)} \quad (10)$$

The eigenstate properties at the edge points of the optical band can then be evaluated as well. The evolutions of the amplitude ratios of the eigenstates on the acoustic and optical bands are provided in [Appendix II](#), from which one can easily identify the amplitude ratios of the eigenstates at the band-edge points. [Table 1](#) summarizes the eigenstate properties at the band-edge points. It is worth noting that there is no band below the first band gap, which means there is no corresponding dynamic eigenstate. In other words, the lower bound of the first band gap corresponds to the static state of the system. [Fig. 3](#) presents the graphical demonstration of the eigenstates listed in [Table 1](#), which reveals more vividly the polarization transition at the band-edges.

The polarization transition observed at the band-edges indicates the topology inversion in the two chain systems with α_1 and α_2 being swapped. Therefore, it can be inferred that when the two chain systems with different topology properties are connected, topological interface states will appear in the two band gaps.

Inspired by the results in [\[26,30\]](#) that negative stiffness springs could generate quasi-static band gaps, in this work, we assume that α_2 (i.e., k_2) could be tuned to negative. If $\alpha_2 < 0$, $\alpha_1 - \alpha_2$ is definitely positive. After swapping the values of α_1 and α_2 , $\alpha_1 - \alpha_2$ will definitely become negative. Therefore, according to the theory presented above, it can be predicted that the band gaps still support the formation of interface states. A negative stiffness device could be realized using a precompressed spring [\[31\]](#), a buckled beam [\[32\]](#), or a shunt circuit piezoelectric transducer [\[26\]](#). However, negative stiffness is often related to physical instability. Before proceeding with

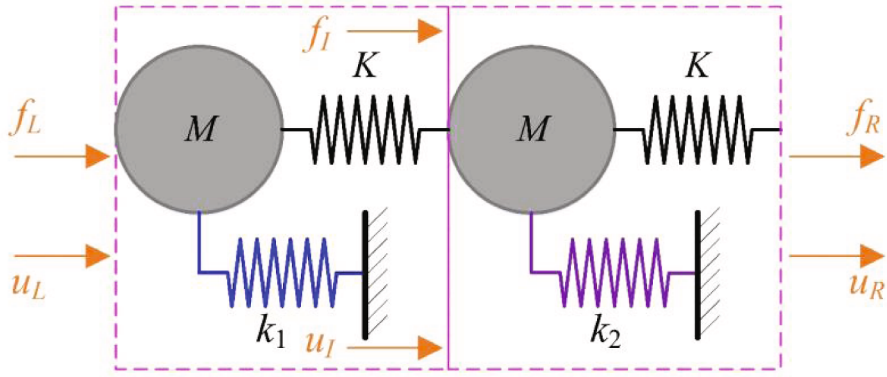


Fig. 4. Schematic of a unit cell of the mass-spring chain with connections to the ground.

the analysis, we need to ascertain the tunable range of α_2 to secure the system stability. For Eq. (6), the solutions can be derived as:

$$\Omega_r^2 = \frac{(\alpha_1 + \alpha_2 + 4) \pm \sqrt{(\alpha_1 - \alpha_2)^2 + 8(1 + \cos(q))}}{2} \quad (11)$$

Once the solution of Ω_r has an imaginary part, it indicates the system becomes unstable. To ensure Ω_r only have real solutions, the right-hand side of Eq. (11) needs to be positive. For the term in the square root operator, we easily know that

$$\max\left(\sqrt{(\alpha_1 - \alpha_2)^2 + 8(1 + \cos(q))}\right) = \sqrt{(\alpha_1 - \alpha_2)^2 + 16} \quad (12)$$

Therefore, the condition of ensuring a positive value at the right-hand side of Eq. (11) becomes:

$$\alpha_2 \geq -\frac{2\alpha_1}{\alpha_1 + 2} \quad (13)$$

We employed the above method to derive the dispersion relation (i.e., Eq. (6)), since it can ease the comparison with the solution of the typical metamaterial (i.e., Eq. (43)) and the derivation of the explicit expression for the stability condition. However, when dealing with a supercell lattice later on, the above method will be difficult to apply because the order of the corresponding coefficient matrix will become quite high and the resultant determinant expression will be complex. Therefore, the transfer matrix method (TMM) is introduced to facilitate the subsequent supercell analysis.

According to the schematic presented in Fig. 4, we can obtain the force/displacement transfer relationship between the left and right-hand side of a unit cell:

$$\begin{cases} -\Omega_r^2 Y_L + (Y_L - Y_I) + \alpha_1 Y_L = -F_L \\ F_I = (Y_I - Y_L) \\ -\Omega_r^2 Y_I + (Y_I - Y_R) + \alpha_2 Y_I = -F_R \\ F_R = (Y_R - Y_I) \end{cases} \quad (14)$$

where F denotes the dimensionless force amplitude, and Y denotes the amplitude of \tilde{y} that follows the same nondimensionlization given in Eq. (2). Writing Eq. (14) in the matrix form gives:

$$\begin{bmatrix} F_R \\ Y_R \end{bmatrix} = \underbrace{\begin{bmatrix} 1 + \alpha_2 - \Omega_r^2 & \alpha_1 - \Omega_r^2 + (\alpha_2 - \Omega_r^2)(1 + \alpha_1 - \Omega_r^2) \\ 2 + \alpha_2 - \Omega_r^2 & \alpha_1 - \Omega_r^2 + (1 + \alpha_2 - \Omega_r^2)(1 + \alpha_1 - \Omega_r^2) \end{bmatrix}}_{\mathbf{T}} \begin{bmatrix} F_L \\ Y_L \end{bmatrix} \quad (15)$$

\mathbf{T} is the transfer matrix. For a supercell lattice, the corresponding total transfer matrix can be obtained from:

$$\begin{bmatrix} F_{\text{LHS}} \\ Y_{\text{LHS}} \end{bmatrix} = \underbrace{\mathbf{T}_1 \mathbf{T}_2 \dots \mathbf{T}_N}_{\mathbf{T}^*} \begin{bmatrix} F_{\text{RHS}} \\ Y_{\text{RHS}} \end{bmatrix} \quad (16)$$

where $\mathbf{T}_1 - \mathbf{T}_N$ represent the transfer matrices of each individual cells that constitute the supercell lattice. The subscripts LHS and RHS denote the left-hand side and the right-hand side ends of the supercell lattice, respectively. To compute the band structure of the supercell lattice, we apply the Bloch's theorem to describe the periodicity. Conforming the transfer matrix \mathbf{T}^* to the periodic condition, i.e., $e^{iq}\mathbf{I}$ (where \mathbf{I} is the identity matrix), an eigenvalue problem is obtained:

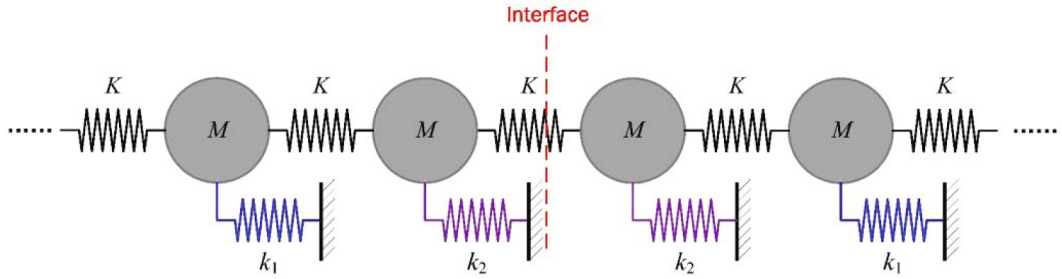


Fig. 5. Schematic of the supercell mass-spring lattice with the interface designed at the middle.

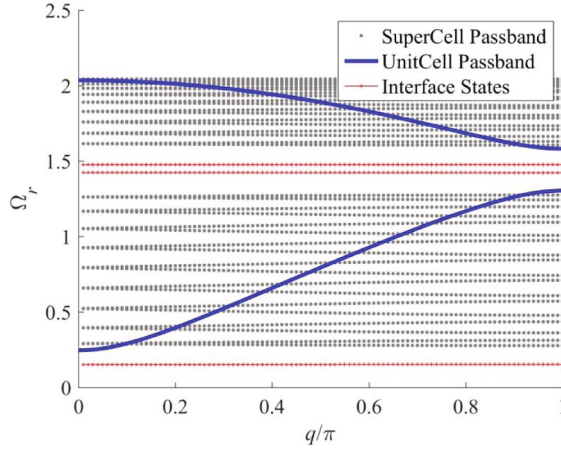


Fig. 6. Band structure of the supercell mass-spring lattice that contains 20 cells. The left 10 cells are configured with \$\alpha_1 = 0.5\$ and \$\alpha_2 = -0.3\$. The right 10 cells are configured with \$\alpha_1 = -0.3\$ and \$\alpha_2 = 0.5\$. The blue solid line denotes the band structure of an ordinary lattice constituted by uniform unit cells. (For interpretation of the references to colour in this figure legend, the reader is referred to the web version of this article.)

$$|\mathbf{T}^* - e^{iq}\mathbf{I}| = 0 \quad (17)$$

Solving Eq. (17) yields the relationship between \$\Omega^*\$ and \$q\$, i.e., the dispersion relation.

To consider a finitely long lattice and calculate its transmittance, one can replace the periodic boundary condition by an appropriate condition, such as:

$$\begin{cases} Y_{\text{LHS}} = 1 \\ F_{\text{RHS}} = 0 \end{cases} \quad (18)$$

We assume the excitation is fed from the left end of the supercell lattice, and its right end is let free. Substituting Eq. (18) into Eq. (16), \$Y_{\text{RHS}}\$ and \$F_{\text{LHS}}\$ can be solved. Thus, the transmittance, i.e., \$\tau\$, could be computed in the unit of dB using the following formula:

$$\tau = 20 \log_{10} \left(\frac{|Y_{\text{RHS}}|}{|Y_{\text{LHS}}|} \right) \quad (19)$$

A supercell lattice that contains 20 cells is constructed, as shown in Fig. 5. The left 10 cells are configured with \$\alpha_1 = 0.5\$ and \$\alpha_2 = -0.3\$. The right 10 cells are configured with \$\alpha_1 = -0.3\$ and \$\alpha_2 = 0.5\$.

Fig. 6 shows the band structure of the supercell lattice. The band structure of an ordinary lattice constituted by uniform unit cells is also provided for comparison. It can be found that the grey-coloured passband curves of the supercell lattice spread over almost the same frequency ranges as those of the ordinary lattice constituted by uniform unit cells. This is because the unit cell components that constitute the supercell lattice actually have the same band structure pattern as that marked in blue in Fig. 6. However, different from the ordinary lattice, several red-coloured flat bands appear in the first and second band gaps of the supercell lattice. These flat bands are the indications of the interface states. Fig. 7(a) presents the calculated transmittance of a single supercell lattice using Eq. (19). The boundary conditions of the supercell lattice are demonstrated in Fig. 7(b) when the excitation is applied from different directions. It is noted that at the same frequencies (i.e., those red-coloured flat lines in Fig. 6 predicted by the supercell band structure analysis, we observe several response peaks formed as the results of interface states. It is worth mentioning that the mass-spring lattice considered in Fig. 6 is an infinitely long system, or in other words, a travelling wave system. However, the mass-spring lattice considered in Fig. 7 (a) is a finitely long system, i.e., a standing wave system. It has a finite number of eigenfrequencies, and thus a finite number of

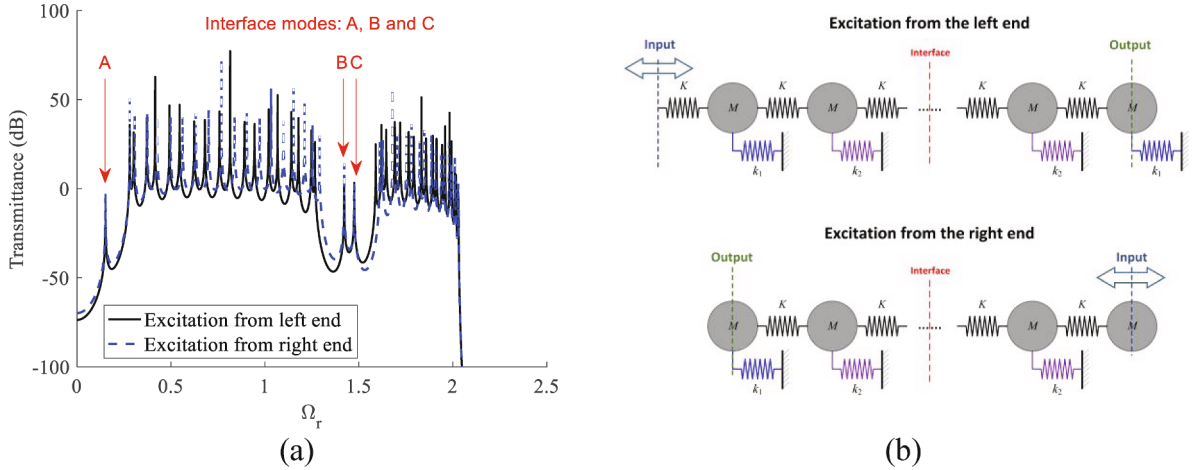


Fig. 7. (a) The transmittance of a single supercell mass-spring lattice with 20 cells. The black solid and the blue dashed lines denote the results computed when the excitation is fed from the left and the right ends, respectively. The red arrows indicate the interface states formed in the band gaps. (b) The boundary conditions of the mass-spring lattice when the excitation is applied from different directions. (For interpretation of the references to colour in this figure legend, the reader is referred to the web version of this article.)

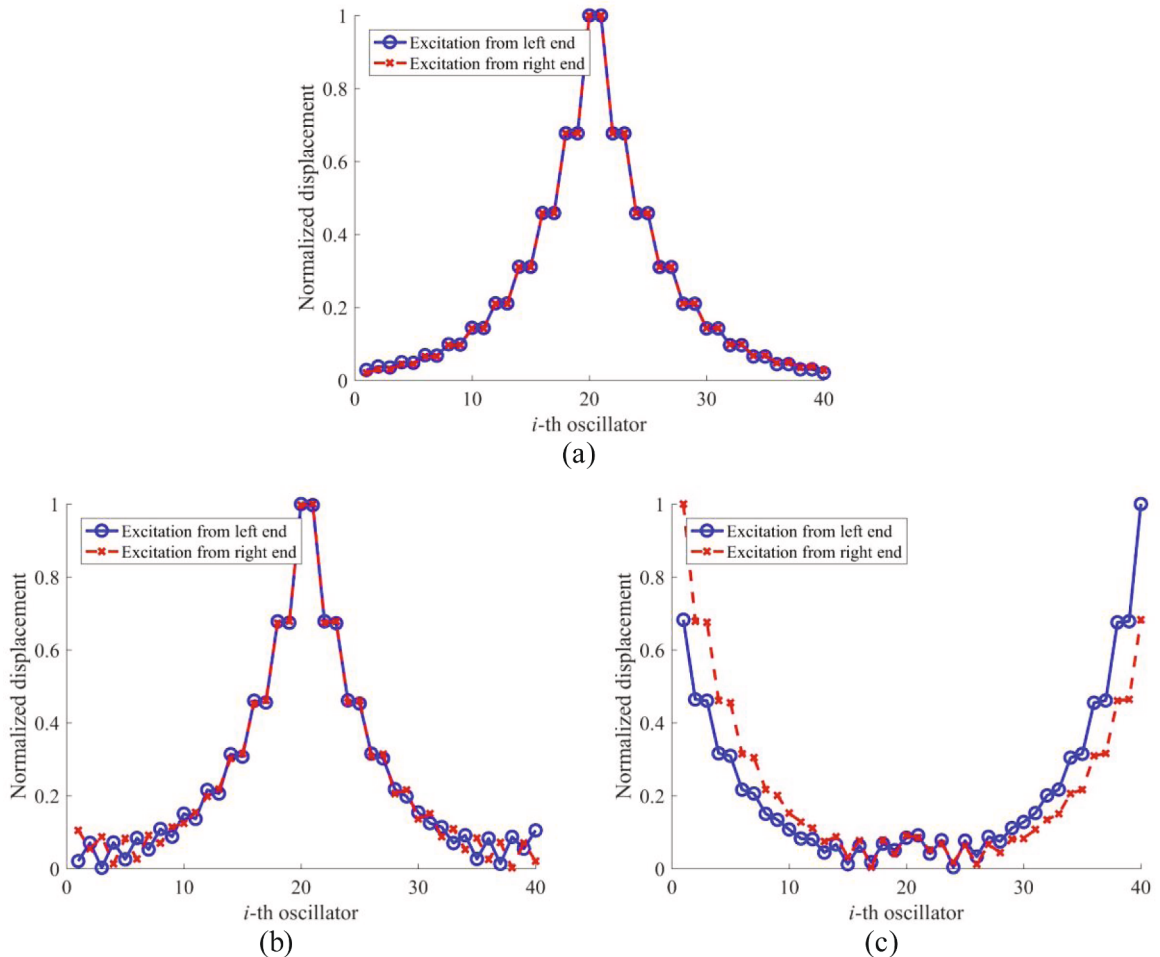


Fig. 8. Displacement distribution along the supercell mass-spring lattice with 20 cells: (a) interface state A; (b) interface state B; (c) interface state C.

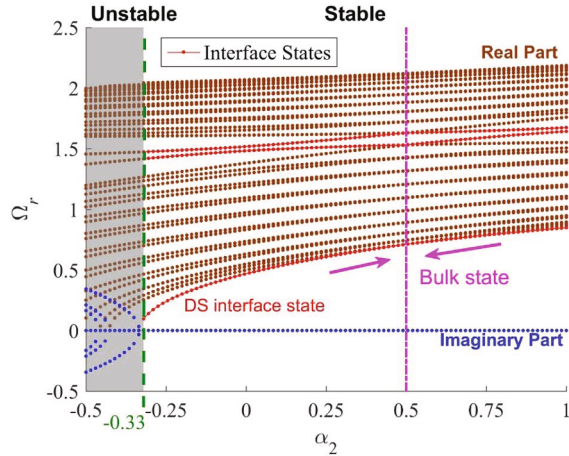


Fig. 9. Evolution of interface states under the influence of α_2 . The brown dots denote the real part solutions and the blue dots denote the imaginary part solutions. The red dots denote the real part solutions that are associated with interface states. (For interpretation of the references to colour in this figure legend, the reader is referred to the web version of this article.)

transmittance peaks. The eigenfrequencies demonstrated in Fig. 6 cannot be related to those transmittance peaks in Fig. 7(a) since they represent different systems. Nonetheless, we can predict the band gap and the formation of interface states in the band structure analysis based on the infinitely long system assumption and the transmittance analysis based on the finitely long system.

For the three interface states illustrated in Fig. 7(a), we plot the corresponding displacement distributions along the supercell lattice in Fig. 8. The vertical axis represents the normalized displacement with respect to the maximum one of all the oscillators in the supercell lattice. It can be seen that the displacement distributions for interface state A (Fig. 8(a)) and interface state B (Fig. 8(b)) are similar, that is, the oscillators near the middle interface have the largest displacement amplitudes. This indicates that the vibration energy is localized at the interface of the supercell lattice since the kinetic energy of an oscillator is proportional to the square of its displacement amplitude. However, for interface state C (Fig. 8(c)), the energy is localized at both edges of the supercell lattice. This is because, from the perspective of the supercell lattice under the assumption of periodic condition, the supercell lattice duplicates periodically in the geometric space [28]. Therefore, both edges of the supercell lattice are also the geometric interfaces where the lattice pattern takes a change. Since the interface states produced in the high-frequency regimes are common and have been widely reported by researchers in many other topological systems, hereinafter, we only focus on investigating the deep-subwavelength (DS) interface state that is formed in the first low-frequency band gap.

As the first band gap starts from 0 Hz, it is naturally wondered that whether it is possible to tune the DS interface state to arbitrarily low frequency. To answer this question, a parametric study is conducted to investigate the dependence of the DS interface state on α_2 . We keep α_1 unchanged since the introduction of the negative stiffness α_2 is the key for producing the DS interface state. Fig. 9 shows the parametric study result. The brown and blue dots denote the real and imaginary parts of the solutions, respectively. According to the stability criterion, once the eigenfrequency solution has a negative imaginary part, it indicates that the system loses stability. From Fig. 9, it is learned that to ensure system stability, α_2 should never be tuned smaller than -0.33 . Note that this critical value is different from that calculated using Eq. (13) (i.e., -0.4). This is because Eq. (13) only applies for an ordinary lattice with uniform unit cells (Fig. 1, and the result presented in Fig. 9 (i.e., -0.33) is for the supercell lattice that contains mixed unit cells. The stability analysis of the supercell lattice is similar to that of the unit cell (i.e., Eq. (13)) and one can follow the similar procedures, since the basic principle for determining the stability is the same.

One can also note in Fig. 9 that with the decrease of α_2 , the corresponding frequency of the DS interface state keeps decreasing. When α_2 approaches the critical value -0.33 , the frequency of the DS interface state becomes quasi-zero. Therefore, the proposed mass-spring topological chain can produce the desired interface state for ultra-low frequency applications. Besides, according to [5], interface states are normally classified into two categories depending on their working frequency domains: 1) the dynamic type that refers to the ones being produced at infinite frequencies; 2) the quasi-static type that refers to the ones working at zero frequency. Theoretically, the proposed mass-spring topological chain system can transform from the dynamic type to the quasi-static type by controlling the parameter α_2 . In addition, it is observed that with the increase of α_2 , the frequency of the DS interface state increases and merges into the bulk states when $\alpha_2 = 0.5 = \alpha_1$. The interface states in the second band gap also exhibit similar behaviours. These phenomena agree with the previous analysis based on Eqs. (7)-(10).

3. Practical structures

In this section, the previous study based on the mass-spring model is extended and applied to design practical structures for producing deep-subwavelength interface states. The following studies focus on the proof-of-concept of the deep-subwavelength interface states in continuous systems. Therefore, the realistic implementation of the negative springs is not discussed in details.

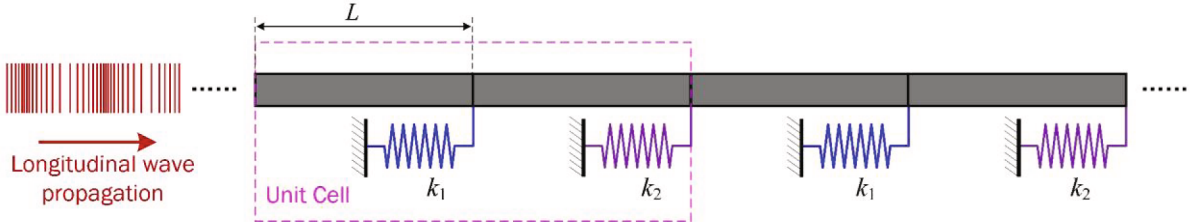


Fig. 10. Longitudinal wave propagates in a rod with periodic spring connections to the ground.

[Appendix III](#) presents two conceptualized physical models and more explanations about the potential solutions for realizing negative springs.

3.1. Longitudinal wave propagation in rod waveguide

First, a rod that supports longitudinal wave propagation is considered. As shown in [Fig. 10](#), a collection of springs are introduced to connect the rod to the ground periodically.

The governing equation of the longitudinal wave propagating in the rod can be written as:

$$EA_{cs} \frac{\partial^2 u(x, t)}{\partial x^2} - \rho A_{cs} \frac{\partial^2 u(x, t)}{\partial t^2} = 0 \quad (20)$$

where E is the Young's modulus of the rod material, ρ is the material density, A_{cs} is the cross-sectional area of the rod, and u is the axial displacement of the rod. It is worth noting that, in general, the dynamic modes of a rod and a beam (that will be investigated later) can involve both tensional (longitudinal) and bending (transverse) displacement components. Under the small deformation assumption, the tensional and bending deformation can be decoupled. In other words, we will only consider the tensional deformation of the rod and the transverse deformation of the beam in this study. By introducing the definitions of the following dimensionless parameters:

$$\left\{ \begin{array}{l} \Omega_L = \frac{\omega}{\sqrt{\frac{EA_{cs}}{\rho A_{cs} L^2}}} \quad \alpha_{1,L} = \frac{k_1}{\left(\frac{EA_{cs}}{L}\right)} \quad \alpha_{2,L} = \frac{k_2}{\left(\frac{EA_{cs}}{L}\right)} \\ \tilde{x} = \frac{x}{L} \quad \tilde{u} = \frac{u}{L} \quad \tilde{t} = t \sqrt{\frac{EA_{cs}}{\rho A_{cs} L^2}} \end{array} \right. \quad (21)$$

[Eq. \(20\)](#) can be non-dimensionalized into the form as:

$$\frac{\partial^2 \tilde{u}(\tilde{x}, \tilde{t})}{\partial \tilde{x}^2} - \frac{\partial^2 \tilde{u}(\tilde{x}, \tilde{t})}{\partial \tilde{t}^2} = 0 \quad (22)$$

Using the variable separation method, one can write $\tilde{u}(\tilde{x}, \tilde{t})$ as

$$\tilde{u}(\tilde{x}, \tilde{t}) = U(\tilde{x}) \exp(i\tilde{\omega}\tilde{t}) \quad (23)$$

where

$$U(\tilde{x}) = A \cos(\Omega_L \tilde{x}) + B \sin(\Omega_L \tilde{x}) \quad (24)$$

Applying the force and displacement continuity conditions at the interface where the spring k_1 is attached, one gets:

$$\left\{ \begin{array}{l} U_i^l(1) = U_j^r(0) \\ \frac{\partial U_i^l(1)}{\partial \tilde{x}} = \frac{\partial U_j^r(0)}{\partial \tilde{x}} - \alpha_{1,L} U_j^r(0) \end{array} \right. \quad (25)$$

Substituting [Eq. \(24\)](#) into [Eq. \(25\)](#) and rewriting the equations into the matrix form, one obtains:

$$\mathbf{H}_{1L} \Psi_i^l = \mathbf{K}_{1L} \Psi_j^r \quad (26)$$

$$\text{where } \Psi_i^l = [A_i^l \quad B_i^l]^T, \Psi_j^r = [A_j^r \quad B_j^r]^T, \mathbf{H}_{1L} = \begin{bmatrix} \cos(\Omega_L) & \sin(\Omega_L) \\ -\sin(\Omega_L) & \cos(\Omega_L) \end{bmatrix}, \mathbf{K}_{1L} = \begin{bmatrix} 1 & 0 \\ -\alpha_{1,L} & 1 \end{bmatrix}.$$

Similarly, the transfer matrix relation is obtained based on the continuity conditions at the interface where the spring k_2 is attached.

Table 2

Geometric and material parameters of the rod and the spring constants.

Parameters	Values	Parameters	Values
Rod segment length	5 cm	Young's modulus	200 GPa
Rod width	1 cm	Mass density	7850 kg/m ³
Rod thickness	1 cm	k_1	4×10^9 N/m
k_2	-2×10^8 N/m		

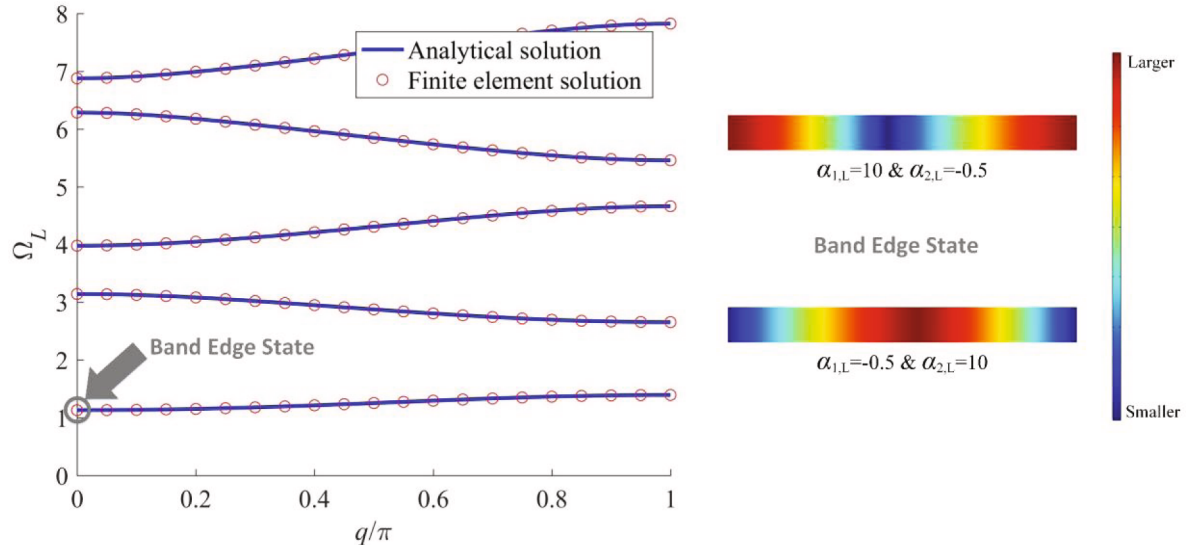


Fig. 11. Comparison of the analytical method and finite element method calculated band structures of a rod with periodic spring connections to the ground. The band-edge states of the longitudinal waveguide when the system parameters are tuned to ($\alpha_{1,L} = 10$ & $\alpha_{2,L} = -0.5$) and ($\alpha_{1,L} = -0.5$ & $\alpha_{2,L} = 10$), respectively.

$$\mathbf{H}_{2L}\Psi_j^r = \mathbf{K}_{2L}\Psi_{i+1}^l \quad (27)$$

where $\Psi_j^r = [A_j^r \ B_j^r]^T$, $\Psi_{i+1}^l = [A_{i+1}^l \ B_{i+1}^l]^T$, $\mathbf{H}_{2L} = \begin{bmatrix} \cos(\Omega_L) & \sin(\Omega_L) \\ -\sin(\Omega_L) & \cos(\Omega_L) \end{bmatrix}$, $\mathbf{K}_{2L} = \begin{bmatrix} 1 & 0 \\ -\frac{\alpha_{2,L}}{\Omega_L} & 1 \end{bmatrix}$. Thus, the left and the right ends of a unit cell are related:

$$\Psi_{i+1}^l = \underbrace{\mathbf{K}_{2L}^{-1}\mathbf{H}_{2L}\mathbf{K}_{1L}^{-1}\mathbf{H}_{1L}}_{\mathbf{T}_L}\Psi_i^l \quad (28)$$

On the other hand, according to the Bloch's theorem, the periodic condition implies:

$$\Psi_{i+1}^l = e^{iq}\Psi_i^l \quad (29)$$

Conforming Eq. (28) to Eq. (29) yields a standard eigenvalue problem:

$$|\mathbf{T}_L - e^{iq}\mathbf{I}| = 0 \quad (30)$$

To compute the transmittance, one only needs to replace the periodic boundary condition by an appropriate condition. In this work, we assume that the rod lattice is under the fixed-free condition.

In the following study, we consider a rod lattice system with the parameters listed in Table 2. According to the defined dimensionless parameters in Eq. (21), one can calculate that $\alpha_{1,L} = 10$ and $\alpha_{2,L} = -0.5$.

For $\alpha_{1,L} = 10$ and $\alpha_{2,L} = -0.5$, the band structure of the longitudinal waveguide constituted by periodically grounded rods is calculated using the analytical method and the finite element method. The results are plotted and compared in Fig. 11. A good agreement is observed between the results of the two methods. When the system parameters are tuned to $\alpha_{1,L} = -0.5$ and $\alpha_{2,L} = 10$, the band structure of the longitudinal waveguide is exactly the same. However, the band-edge states for the two configurations, as illustrated on the right-hand side of Fig. 11, are different. The polarization directions of the mode shapes are inverted. Note that the first band gap starts from 0 Hz. It implies that at the lower bound (i.e., 0 Hz) of the first band gap, the wave modes in both configurations undergo the quasi-static free motion. Therefore, from the lower to the upper bound of the first band gap, the wave modes in

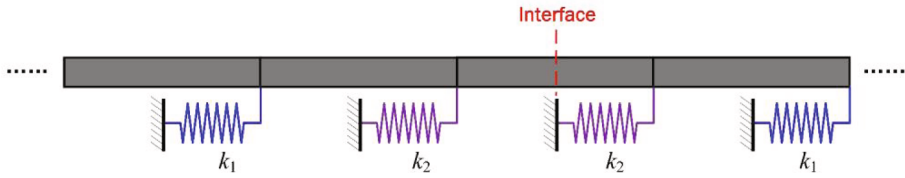


Fig. 12. Schematic of the supercell rod lattice with the interface designed at the middle.

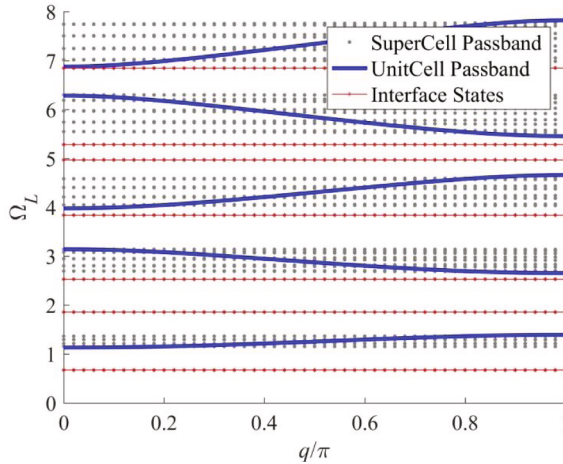


Fig. 13. Band structure of the supercell rod lattice that consists of 10 cells. The left-hand side five cells with parameters of $\alpha_{1,L} = 10$ & $\alpha_{2,L} = -0.5$; and the right-hand side five cells with parameters of $\alpha_{1,L} = -0.5$ & $\alpha_{2,L} = 10$.

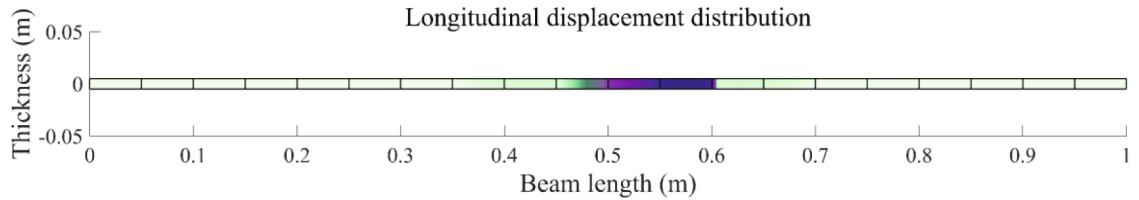


Fig. 14. Mode shape of the supercell rod lattice at the DS interface state.

the two configurations, separately, evolve toward different polarization patterns. It is inferred that the polarization inversion could open the opportunity to form an interface state in a system that consists of mixed configurations with different polarization features on the left and right halves.

To produce a DS interface state in the rod waveguide, a supercell rod lattice shown in Fig. 12 is constructed with the left-hand side five cells being tuned of $\alpha_{1,L} = 10$ & $\alpha_{2,L} = -0.5$ and the right-hand side five cells of $\alpha_{1,L} = -0.5$ & $\alpha_{2,L} = 10$. Fig. 13 shows the band structure of the supercell rod lattice. The solid blue lines denote the passbands of an ordinary rod waveguide with a uniform configuration. As expected, the grey-coloured passbands of the supercell lattice spread over almost the same frequency ranges as those blue-coloured passbands of the uniform waveguide. Similar to the phenomenon in the mass-spring model, several red-coloured flat bands appear in the band gaps of the supercell rod lattice, indicating the formation of interface states. Since the DS interface state (at the frequency of $\Omega_L = 0.67$, ≈ 10800 Hz for the system with given parameters listed in Table 2) is the most interested, its corresponding mode shape is examined in Fig. 14. The colour depth represents the displacement amplitude. The deeper the colour, the larger the displacement amplitude is. The mode shape clearly demonstrates that the energy concentrates at the interface of the supercell rod lattice.

Assuming the ground is at the absolutely static status, and the base excitation only comes from the left end, the transmittance of a single supercell rod lattice (i.e., with finitely long length) is calculated and plotted in Fig. 15(a). When the excitation is input from the right end, the transmittance spectra are similar, thus they are not presented in Fig. 15(a) to avoid confusion. The black solid and blue dash-dotted lines represent the transmittances of the tip and the middle of the supercell rod lattice, respectively. In the valleys of the transmittance curve which are formed due to the band gap effect, resonant peaks (i.e., $\Omega_L = 0.675, 1.855, 3.84, 4.965$) are found at the identical frequencies of the interface states predicted by the supercell band structure analysis (i.e., Fig. 13. However, though there exists a resonant peak in the first band gap formed valley, the absolute transmittance value is actually small.

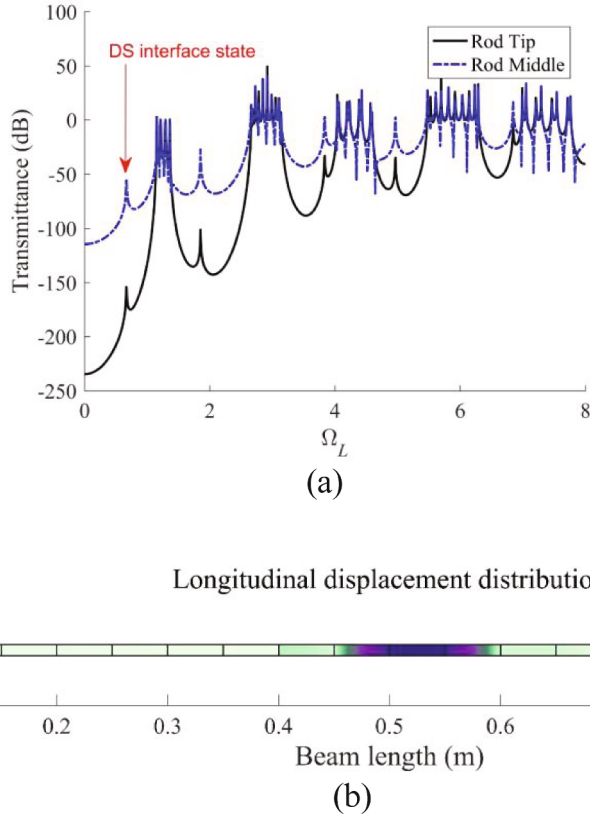


Fig. 15. Under the base excitation from the left end of a single supercell rod lattice and the ground is at the absolutely static status. (a) The transmittance of the single supercell rod lattice; (b) the displacement distribution contour at the first resonant peak of the transmittance spectrum.

Fig. 15(b) presents the longitudinal displacement distribution of the supercell rod lattice at the DS interface state. Since the interface state formed resonant peak is bogged down in the first deep valley, the displacement amplitudes along the first 4 cells and the latter 6 cells of the supercell rod lattice are scaled by different factors to intentionally demonstrate the energy distribution profile around the interface. Along the first 4 cells, the vibration energy quickly decreases due to the vibration suppression effect of the band gap. For a conventional non-topological lattice, the vibration energy along the latter 6 cells should decrease monotonously. However, due to the interface state formation, along the rest of the supercell rod lattice, the energy appears to stream to the middle interface.

In a different circumstance, we regard the ground as the general base. The left end of the supercell rod lattice is rigidly linked to the general base as well. The detailed differences between this type of base excitation condition and the previous one, which considers the ground at the absolutely static status, are explained in Appendix IV. When an excitation is applied, Fig. 16(a) presents the transmittance of the supercell rod lattice. It is found that under this situation, the first valley disappears in the transmittance spectrum. Nonetheless, over the first band gap frequency range, only an unnoticeable peak (which can not be observed in the figure at the current scale) is formed in the transmittance spectrum measured at the tip (i.e., right-hand side end) of the supercell rod lattice. On the other hand, by examining the middle interface of the supercell rod lattice, a sharp resonant peak (i.e., at $\Omega_L = 0.67$) in the transmittance spectrum is observed. The sharp resonant peak is just at the same frequency of the interface state predicted in Fig. 13. Fig. 16(b) shows the corresponding longitudinal displacement distribution of the supercell rod lattice at that resonant frequency. Note that a consistent factor scales the displacement amplitudes along the entire supercell rod lattice. It can be seen that the displacement distribution strictly follows the mode shape of the interface state as presented in Fig. 14. Therefore, we can conclude that provided the topological structure is unchanged, the interface state still appears even if the excitation condition is varied.

To investigate the dependence of the DS interface state of the supercell rod lattice, $\alpha_{1,L}$ is kept unchanged. Fig. 17 reveals the evolution of the DS interface state as $\alpha_{2,L}$ is varied in the negative regime. In consistency with the convention in Section 2, the brown and blue dots represent the real and imaginary parts of the solutions, respectively. Based on the principle of stability determination, one knows that $\alpha_{2,L}$ should not be tuned smaller than -0.9 for guaranteeing the system stability. Within the stable regime, it is noted that when $\alpha_{2,L}$ keeps decreasing to approach the critical value -0.9 , the frequency of the DS interface state monotonously decreases until quasi-zero. Therefore, the conclusions for the mass-spring model are still valid for the rod model, i.e.: 1) the DS interface state could be tuned to arbitrarily ultra-low frequency; 2) the DS interface state in the topological rod lattice can transform from the dynamic type to the quasi-static type.

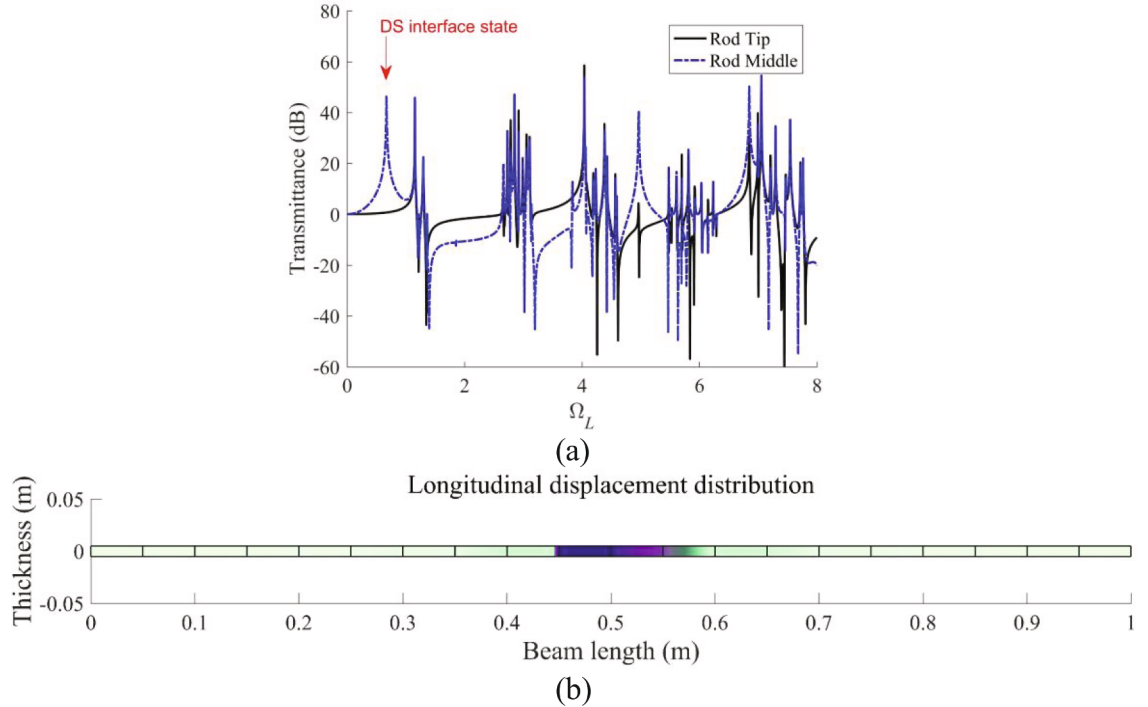


Fig. 16. Under the base excitation from the left end of a single supercell rod lattice and the ground is regarded as the general base. (a) The transmittance of the single supercell rod lattice; (b) the displacement distribution contour at the first resonant peak of the transmittance spectrum.

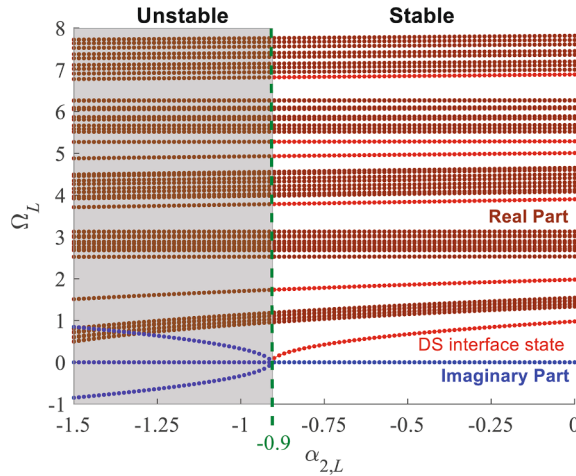


Fig. 17. Evolution of interface states under the influence of $\alpha_{2,L}$. The brown dots denote the real part solutions and the blue dots denote the imaginary part solutions. The red dots denote the real part solutions that are associated with interface states. (For interpretation of the references to colour in this figure legend, the reader is referred to the web version of this article.)

3.2. Transverse wave propagation in beam waveguide

In the second case, the transverse wave propagation in a beam structure is considered. The beam is periodically connected to the ground by vertically placed springs, as demonstrated in Fig. 18.

Based on the Euler's beam theory, the governing equation of the transverse vibration is written as:

$$\rho A_{cs} \frac{\partial^2 w(x, t)}{\partial t^2} + EI_{cs} \frac{\partial^4 w(x, t)}{\partial x^4} = 0 \quad (31)$$

where I_{cs} is the second moment of area of the beam, and w is the transverse displacement of the beam. The below dimensionless parameters are defined:

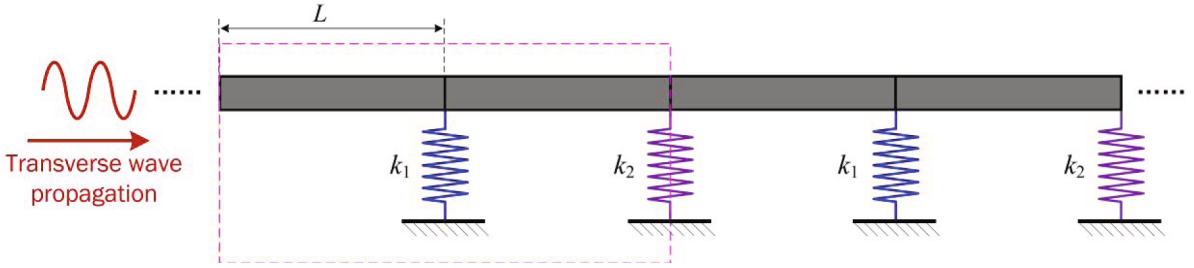


Fig. 18. Transverse wave propagates in a beam with periodic spring connections to the ground.

$$\left\{ \begin{array}{l} \Omega_T = \frac{\omega}{\sqrt{\rho A_{cs} L^4}} \quad \alpha_1 = \frac{k_1}{\left(\frac{EI_{cs}}{L^3}\right)} \quad \alpha_2 = \frac{k_2}{\left(\frac{EI_{cs}}{L^3}\right)} \\ \tilde{x} = \frac{x}{L} \quad \tilde{w} = \frac{w}{L} \quad \tilde{t} = t \sqrt{\frac{EI_{cs}}{\rho A L^4}} \end{array} \right. \quad (32)$$

The beam governing equation, i.e., Eq. (31), is non-dimensionalized as:

$$\frac{\partial^2 \tilde{w}(\tilde{x}, \tilde{t})}{\partial \tilde{t}^2} + \frac{\partial^4 \tilde{w}(\tilde{x}, \tilde{t})}{\partial \tilde{x}^4} = 0 \quad (33)$$

We separate the variable $\tilde{w}(\tilde{x}, \tilde{t})$ in the form as $W(\tilde{x})\exp(i\tilde{t})$, where

$$W(\tilde{x}) = A\cos(\beta\tilde{x}) + B\sin(\beta\tilde{x}) + C\cosh(\beta\tilde{x}) + D\sinh(\beta\tilde{x}) \quad (34)$$

in which $\beta^4 = \Omega_T^2$. The slope is proportional to the first derivative of the deflection. The shear force and the moment are proportional to the third and second derivatives of the deflection, respectively. The internal shear force in the beam is required to balance the external force applied by the spring that is connected to the ground. Therefore, the displacement, slope, moment, and force continuity conditions at the interface where the spring k_1 is attached are formulated as [33]:

$$\left\{ \begin{array}{l} W_i^l(1) = W_j^r(0) \\ \frac{\partial W_i^l(1)}{\partial x} = \frac{\partial W_j^r(0)}{\partial x} \\ \frac{\partial^2 W_i^l(1)}{\partial x^2} = \frac{\partial^2 W_j^r(0)}{\partial x^2} \\ \frac{\partial^3 W_i^l(1)}{\partial x^3} = \frac{\partial^3 W_j^r(0)}{\partial x^3} + \alpha_1 W_j^r(0) \end{array} \right. \quad (35)$$

Substituting Eq. (34) into Eq. (35) yields:

$$\mathbf{H}_1 \Psi_i^l = \mathbf{K}_1 \Psi_j^r \quad (36)$$

where $\Psi_i^l = [A_i^l \quad B_i^l \quad C_i^l \quad D_i^l]^T$, $\Psi_j^r = [A_j^r \quad B_j^r \quad C_j^r \quad D_j^r]^T$,

$$\mathbf{H}_1 = \begin{bmatrix} \cos(\beta) & \sin(\beta) & \cosh(\beta) & \sinh(\beta) \\ -\sin(\beta) & \cos(\beta) & \sinh(\beta) & \cosh(\beta) \\ -\cos(\beta) & -\sin(\beta) & \cosh(\beta) & \sinh(\beta) \\ \sin(\beta) & -\cos(\beta) & \sinh(\beta) & \cosh(\beta) \end{bmatrix} \mathbf{K}_1 = \begin{bmatrix} 1 & 0 & 1 & 0 \\ 0 & 1 & 0 & 1 \\ -1 & 0 & 1 & 0 \\ \frac{\alpha_1}{\beta^3} & -1 & \frac{\alpha_1}{\beta^3} & 1 \end{bmatrix} \quad (37)$$

Similarly, the continuity conditions at the interface where the spring k_2 is attached are formulated as:

$$\mathbf{H}_2 \Psi_j^r = \mathbf{K}_2 \Psi_{i+1}^l$$

$$\text{where } \Psi_j^r = [A_j^r \quad B_j^r \quad C_j^r \quad D_j^r]^T, \Psi_{i+1}^l = [A_{i+1}^l \quad B_{i+1}^l \quad C_{i+1}^l \quad D_{i+1}^l]^T, \mathbf{H}_2 = \mathbf{H}_1, \mathbf{K}_2 = \begin{bmatrix} 1 & 0 & 1 & 0 \\ 0 & 1 & 0 & 1 \\ -1 & 0 & 1 & 0 \\ \frac{\alpha_2}{\beta^3} & -1 & \frac{\alpha_2}{\beta^3} & 1 \end{bmatrix}$$

Table 3

Geometric and material parameters of the rod and the spring constants.

System parameters	values	System parameters	values
Beam segment length	5 cm	Young's modulus	200 GPa
Beam width	1.4 cm	Mass density	7850 kg/m ³
Beam thickness	2 mm	k_1	74667 N/m
k_2	-14933 N/m		

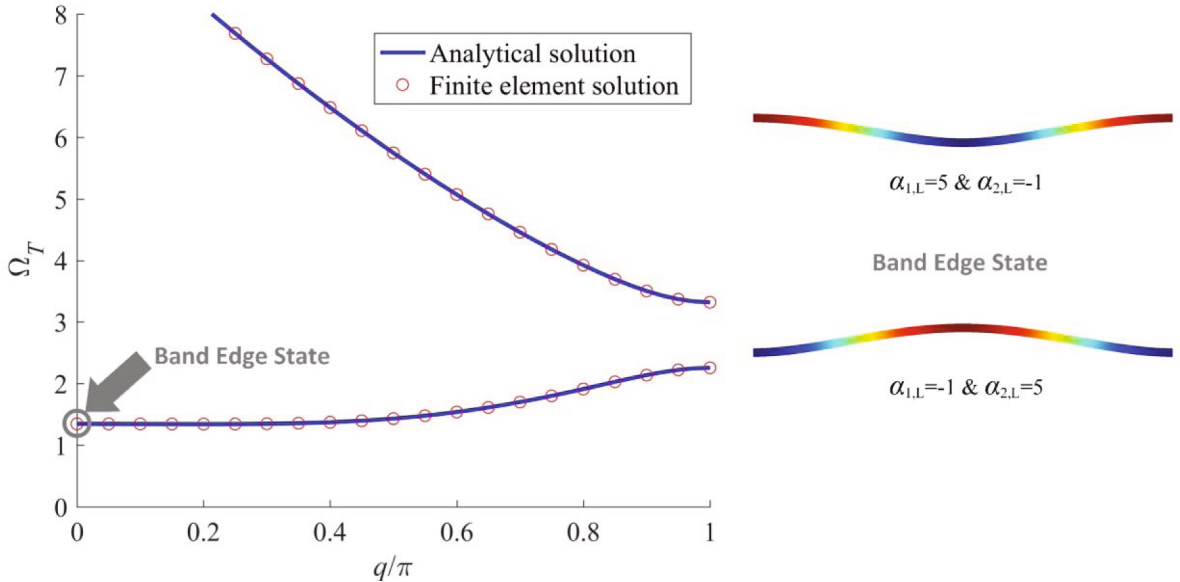


Fig. 19. Comparison of the analytical method and finite element method calculated band structures of a beam with periodic spring connections to the ground. The band-edge states of the transverse waveguide when the system parameters are tuned to ($\alpha_{1,T} = 5$ & $\alpha_{2,T} = -1$) and ($\alpha_{1,L} = -1$ & $\alpha_{2,L} = 5$), respectively.

The right and the left ends of a unit cell are thus related by:

$$\Psi_{i+1}^l = \underbrace{\mathbf{K}_2^{-1} \mathbf{H}_2 \mathbf{K}_1^{-1} \mathbf{H}_1}_{\mathbf{T}_T} \Psi_i^l \quad (38)$$

When a transverse wave travels in the beam waveguide with infinite length, the geometric periodicity implies the below relation equation:

$$\Psi_{i+1}^l = e^{iq} \Psi_i^l \quad (39)$$

Mediating between Eq. (38) and Eq. (39) leads to a standard eigenvalue problem:

$$|\mathbf{T}_T - e^{iq} \mathbf{I}| = 0 \quad (40)$$

Eq. (40) depicts the relation between the frequency and the wavenumber of the transverse wave that travels in the beam waveguide. To consider a finitely long beam lattice, one needs to replace the periodic boundary condition by such as the fixed-free boundary condition, as we did for the mass-spring model. Table 3 lists the parameters of the beam and the constants of the springs. According to the defined dimensionless parameters (i.e., Eq. (32)), one can determine that $\alpha_{1,T} = 5$ and $\alpha_{2,T} = -1$.

For the transverse waveguide tuned with parameters of $\alpha_{1,T} = 5$ and $\alpha_{2,T} = -1$, Fig. 19 presents the corresponding band structure. The finite element result is also provided, which tightly matches the analytical result. The band structure for the transverse waveguide with parameters of $\alpha_{1,T} = -1$ and $\alpha_{2,T} = 5$ remains the same. However, the band-edge states for the two configurations are different. As demonstrated on the right-hand side of Fig. 19, the mode shape deflection directions are opposite for the two configurations. Due to the similar mechanism as explained for the longitudinal waveguide, the polarization inversion of the wave mode has the potential to be employed to produce an interface state in the first band gap of a well-engineered transverse waveguide.

Following the same design strategy used before, a supercell beam lattice shown in Fig. 20 is constructed to form a DS interface state. There are 20 unit cells in total. The left 10 cells of the supercell lattice are uniformly configured with $\alpha_{1,T} = 5$ and $\alpha_{2,T} = -1$. The right 10 cells are consistently tuned with $\alpha_1 = -1$ and $\alpha_2 = 5$. Fig. 21 shows the band structure analysis result of the supercell beam lattice. Just as in the previous models, the grey-coloured passbands of the supercell beam lattice span over almost the same frequency range as

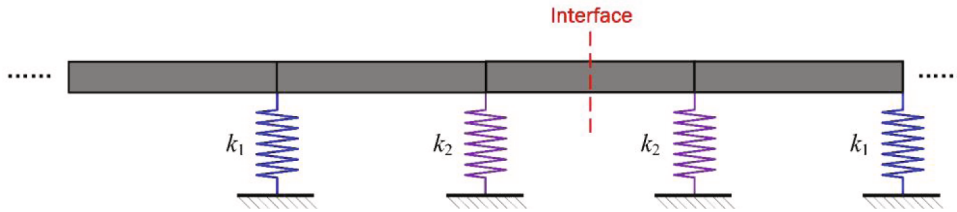


Fig. 20. Schematic of the supercell beam lattice with the interface designed at the middle.

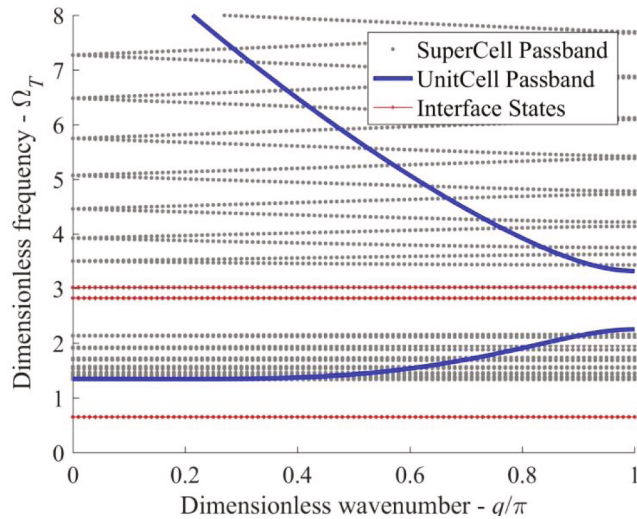


Fig. 21. Band structure of the supercell beam lattice that consists of 20 cells. The left-hand side 10 cells with parameters of $\alpha_{1,T} = 5$ & $\alpha_{2,T} = -1$; and the right-hand side 10 cells with parameters of $\alpha_{1,T} = -1$ & $\alpha_{2,T} = 5$.

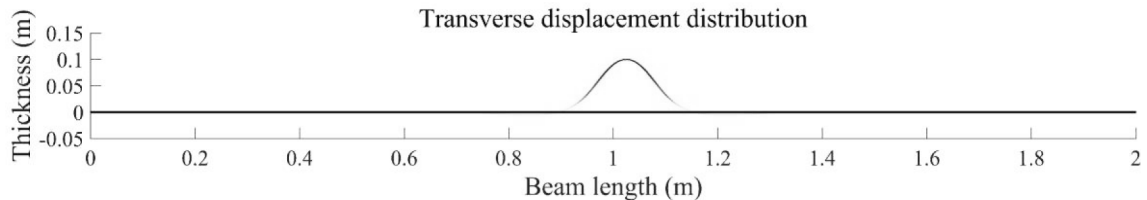


Fig. 22. Mode shape of the supercell beam lattice at the DS interface state. Note that the transverse displacement is scaled by a factor and does not reflect the true deformation.

the blue-coloured passbands of the uniform beam lattice. Several red-coloured flat bands, which are the indications of interface states, appear in the band gaps of the supercell beam lattice. The DS interface state is formed at the frequency of $\Omega_T = 0.65$, which is about 120.8 Hz for the system with the parameters given in Table 3.

As the DS interface state ($\Omega_T=0.65$) in the ultra-low frequency band gap is of the most interest, we plot the corresponding mode shape of the supercell beam lattice in Fig. 22. A familiar energy localization phenomenon is observed at the geometric interface of the supercell beam lattice.

Similar to Section 3.1, we first consider that the ground is at the absolutely static status, and the excitation is input from the left end of a single supercell beam lattice (i.e., with finite length). The transmittance of the supercell beam lattice is plotted in Fig. 23(a). As was foreseeable, we note a resonant peak in the transmittance spectrum at the interface state frequency ($\Omega_T=0.65$) predicted by the band structure analysis of the supercell beam lattice. Fig. 23(b) shows the displacement distribution along the supercell beam lattice at the DS interface state induced resonant frequency. Since the left end is the input terminal of the excitation, the high vibration energy distribution on the left end is easily understandable. Note that the displacement distributions along the first 7 cells and the subsequent 13 cells are scaled by different factors. Otherwise, the entire beam displacement distribution would be almost flat, except around the left end from where the excitation is input. After the scaling treatment, it can be found that the vibration energy first decreases rapidly, then concentrates at the middle interface of the supercell beam lattice. The energy localization phenomenon at the middle interface can

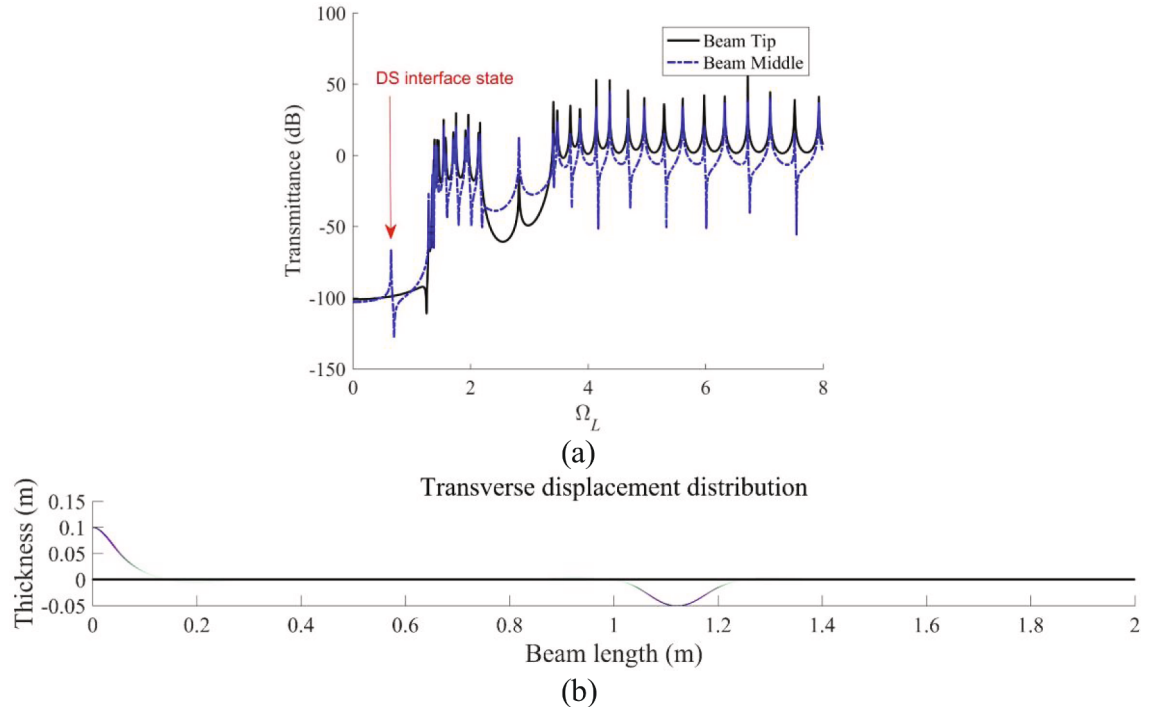


Fig. 23. Under the base excitation from the left end of a single supercell beam lattice and the ground is at the absolutely static status. (a) The transmittance of the supercell rod lattice; (b) the displacement distribution contour at the first resonant peak of the transmittance spectrum.

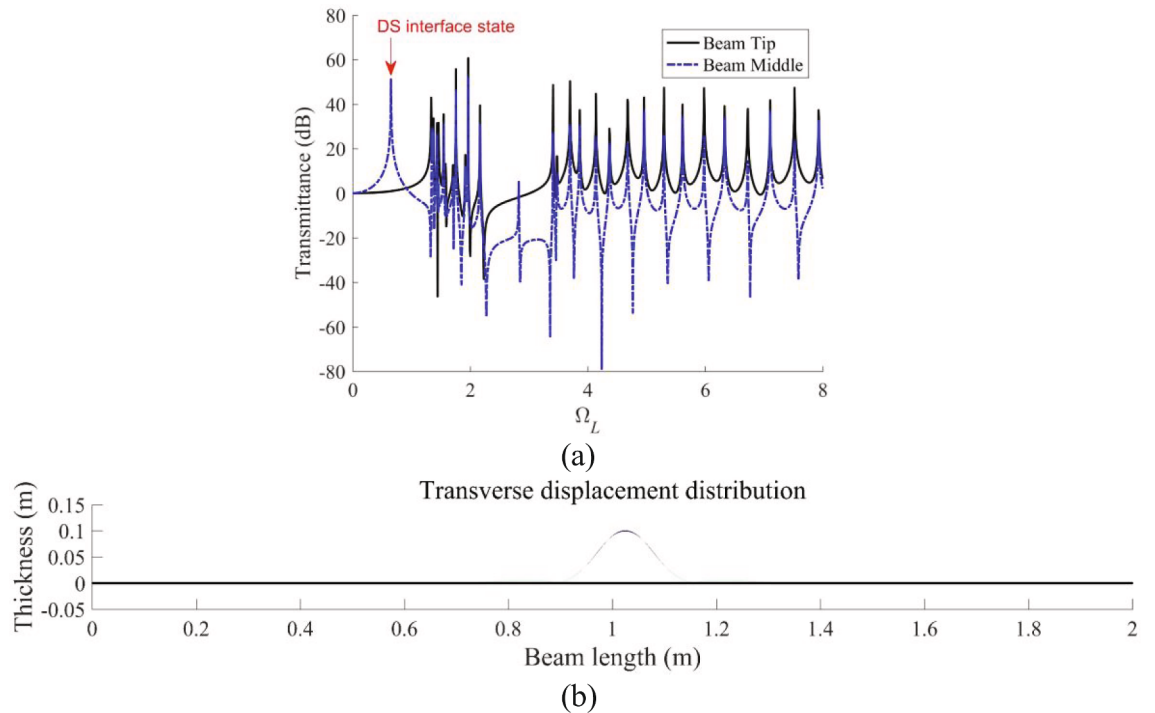


Fig. 24. Under the base excitation from the left end of a single supercell beam lattice and the ground is regarded as the general base. (a) The transmittance of the supercell rod lattice; (b) the displacement distribution contour at the first resonant peak of the transmittance spectrum.

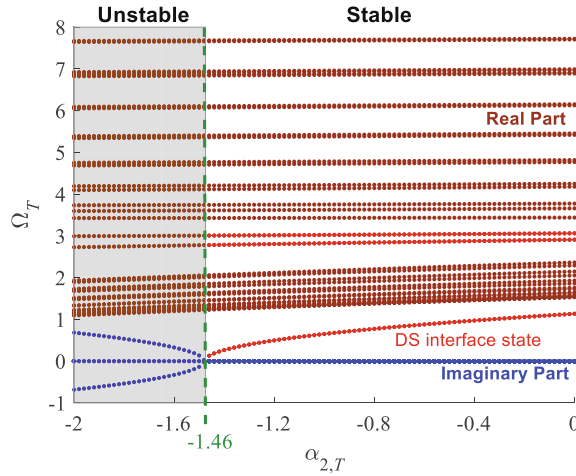


Fig. 25. Evolution of interface states under the influence of $\alpha_{2,T}$. The brown dots denote the real part solutions and the blue dots denote the imaginary part solutions. The red dots denote the real part solutions that are associated with interface states. (For interpretation of the references to colour in this figure legend, the reader is referred to the web version of this article.)

be explained by the interface state mechanism.

Subsequently, we consider another circumstance and regard the ground as the general base. The detailed differences between this type of base excitation condition and the previous one, which considers the ground at the absolutely static status, are explained in Appendix IV. Under a given base excitation, i.e., the inertial coordinate is vibrating, Fig. 24(a) presents the transmittance of the supercell beam lattice. Since the entire structure is under a field excitation, the first valley in the transmittance spectrum disappears. Although the band gap effect does not work under such excitation, over the corresponding frequency range in the transmittance spectrum measured at the tip of the supercell beam lattice, resonant peaks are prevented from being formed. However, when we measure the transmittance spectrum at the middle interface of the supercell beam lattice, a single sharp resonant peak is noted at $\Omega_T = 0.65$ where the band gap should have been located. The frequency that corresponds to the sharp resonant peak is just identical to the DS interface state frequency predicted in Fig. 21. To further unveil the formation mechanism of that resonant peak, the displacement distribution along the entire supercell beam lattice is examined in Fig. 24(b). The displacement amplitudes along the entire supercell beam lattice are scaled by a consistent factor. By comparing Fig. 24(b) with Fig. 22, it is evident that the resonance is induced by the activation of the DS interface state. In retrospect to the above analysis procedures, it is recognized that including the ground as the general base only alters the excitation condition. Therefore, it is not surprising to find that only the interface state can be activated over the first band gap frequency range, and only a corresponding resonant peak can form in the transmittance spectrum.

Following the same procedure, we keep $\alpha_{1,T}$ unchanged and vary $\alpha_{2,T}$ to investigate its influence on the formation of the DS interface state. Fig. 25 presents the corresponding results. Again, the brown and blue dots, respectively, denote the real and imaginary parts of the solutions. By inspecting the imaginary part, it is easy to know that the stable regime of the supercell beam lattice is $\alpha_{2,T} > -1.46$. Within the stable regime, one notes that with the decrease of $\alpha_{2,T}$, the DS interface state tends to form at a lower frequency. When $\alpha_{2,T}$ is tuned to be very close to the critical value -1.46 , the DS interface state is almost transformed into the quasi-static type: the working frequency is nearly 0 Hz.

4. Conclusions

This paper has proposed a topological mechanical system for producing an ultra-low frequency interface state. A mass-spring model has been first adopted for proof-of-concept. All the mass particles in the chain have been proposed to be connected to the ground by springs. The dispersion relations of the mass-spring model and the supercell lattice have been derived. The band gap characteristics have been discussed, and the quasi-static band gap has been identified as the locally resonant type. The stability of the system has been examined. It has been found that within the stable regime, by making the topological invariants in the two halves of the mass-spring chain different, an interface state can be produced in the quasi-static band gap. Moreover, it has been proven that the interface state can be formed at an arbitrarily low frequency by carefully configuring the spring connections to the ground. We have also proposed two practical systems based on rod and beam structures. Using the transfer matrix method, the dispersion relations of the practical systems have been derived as well. Through modal analyses and frequency domain analyses, the deep-subwavelength interface states in both topological structures have been ascertained. The interface state formation behaviours in the mass-spring model and continuous rod and beam models have been found to be qualitatively similar: the corresponding frequency can be tuned to arbitrarily low frequency. Therefore, our study has provided an effective means for achieving deep-subwavelength interface states in mechanical systems.

CRediT authorship contribution statement

Guobiao Hu: Conceptualization, Methodology, Software, Validation, Formal analysis, Investigation, Writing – original draft. **Chunbo Lan:** Formal analysis, Investigation, Writing – review & editing. **Lihua Tang:** Formal analysis, Investigation, Writing – review & editing. **Yaowen Yang:** Formal analysis, Investigation, Writing – review & editing, Supervision.

Declaration of Competing Interest

The authors declare that they have no known competing financial interests or personal relationships that could have appeared to influence the work reported in this paper.

Appendix I

The first band gap in Fig. 2 is formed due to the local resonance mechanism. To help understand this, a similar but more typical locally resonant metamaterial (as shown in Fig. 26) is considered first. Instead of connecting to the ground, each particle in the host chain is attached with a local resonator of mass m . The motion equations of the particles in a representative unit cell can be written as:

$$\begin{cases} M\ddot{y}_i + K(y_i - y_{i-1}) + K(y_i - y_j) + k_1(y_i - z_i) = 0 \\ m\ddot{z}_i + k_1(z_i - y_i) = 0 \\ M\ddot{y}_j + K(y_j - y_i) + K(y_j - y_{i+1}) + k_2(y_j - z_j) = 0 \\ m\ddot{z}_j + k_2(z_j - y_j) = 0 \end{cases} \quad (41)$$

where z represents the displacement of the local resonator. By introducing two additional dimensionless parameters, i.e., $\tilde{z}_j = z_j/L$ and $\mu = m/M$, we can non-dimensionlize Eq. (41). Applying the Fourier's transform, we can obtain the non-dimensionlized Eq. (41)

$$\begin{cases} -\Omega_r^2 Y_i + (2Y_i - Y_{i-1} - Y_j) + \alpha_1(Y_i - Z_i) = 0 \\ -\mu\Omega_r^2 Z_i + \alpha_1(Z_i - Y_i) = 0 \\ -\Omega_r^2 Y_j + (2Y_j - Y_i - Y_{i+1}) + \alpha_2(Y_j - Z_j) = 0 \\ -\mu\Omega_r^2 Z_j + \alpha_2(Z_j - Y_j) = 0 \end{cases} \quad (42)$$

Using the Bloch's theorem to describe the periodicity and following the similar procedures, we obtain the dispersion relation of the elastic waves propagating in the locally resonant metamaterial:

$$\begin{aligned} -\Omega^8 + \left[(\alpha_1 + \alpha_2 + 4) + \frac{(\alpha_1 + \alpha_2)}{\mu} \right] \Omega^6 - \left\{ \begin{array}{l} [\alpha_1 \alpha_2 + 2(\alpha_1 + \alpha_2) + 2(1 - \cos(q))] \\ + \frac{2(2 + \alpha_1)(\alpha_1 + \alpha_2)}{\mu} + \frac{\alpha_1 \alpha_2}{\mu^2} \end{array} \right\} \Omega^4 \\ + \left\{ \begin{array}{l} \frac{[2\alpha_1^2 \alpha_2 + (4\alpha_1 + 2 - 2\cos(q))(\alpha_1 + \alpha_2)]}{\mu} \\ + \frac{2\alpha_1^2 \alpha_2 + 4\alpha_1 \alpha_2}{\mu^2} \end{array} \right\} \Omega^2 - \frac{4\alpha_1^2 \alpha_2 + [2 - 2\cos(q)]\alpha_1 \alpha_2}{\mu^2} = 0 \end{aligned} \quad (43)$$

It is noted that when the mass of the local resonator, i.e., m , approaches positive infinite, μ becomes infinite, and Eq. (43) degenerates into Eq. (6). This complies with the fact that the mass of the ground foundation is infinite. In other words, the mass-spring

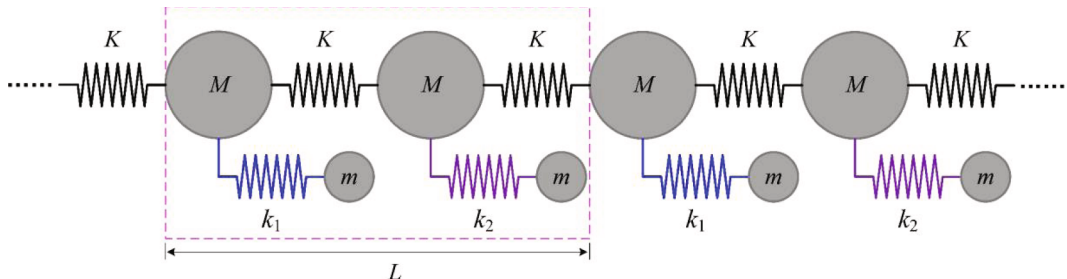


Fig. 26. Schematic of a locally resonant metamaterial.

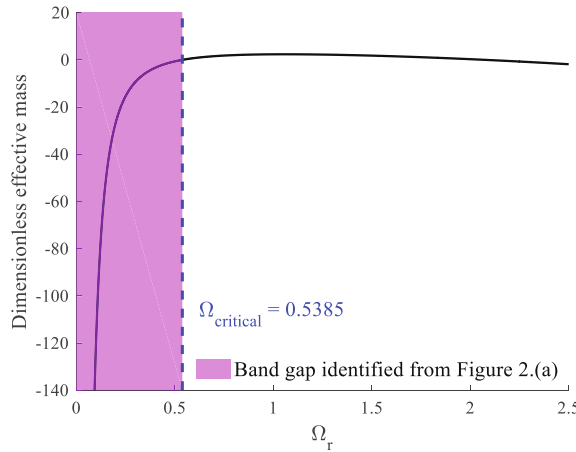


Fig. 27. Dimensionless effective mass of the particle versus dimensionless frequency.

chain with connections to the ground can be regarded as a special type of metamaterial with the local resonator mass of infinity. On the other hand, according to the fundamental mechanism of locally resonant metamaterials, once the effective mass becomes negative, the acceleration appears in the opposite direction to the applied force, and the response amplitude would be reduced. From this perspective, we can derive and examine the effective mass of the particle that is connected to the ground through a spring. If the effective mass of the grounded particle is negative in the first band gap, then we can conclude that it is a local resonance induced band gap. We first consider an ordinary mass-spring model without spring connections to the ground. The dispersion relation can be derived to be:

$$\Omega_r^2 = \frac{2[1 - \cos(q)]}{\hat{M}_{eff}} \quad (44)$$

where $\hat{M}_{eff} = M_{eff}/M$, and M_{eff} is the mass of the particle. Subsequently, we intentionally force the ordinary mass-spring model to have the same dispersion relation as Eq. (6). The effective mass of the particle is required to be:

$$\hat{M}_{eff} = (\alpha_1 + \alpha_2 + 4) - \Omega_r^2 - \frac{\alpha_1 \alpha_2 + 2(\alpha_1 + \alpha_2)}{\Omega_r^2} \quad (45)$$

According to Eq. (45), one knows that when $\Omega_r < \Omega_{critical}$, \hat{M}_{eff} is negative.

$$\Omega_{critical} = \sqrt{\frac{(\alpha_1 + \alpha_2 + 4) - \sqrt{(\alpha_1 + \alpha_2 + 4)^2 - 4[\alpha_1 \alpha_2 + 2(\alpha_1 + \alpha_2)]}}{2}} \quad (46)$$

Fig. 27 plots the dimensionless effective mass of the particle calculated using Eq. (45). The first band gap range identified from the band structure presented in Fig. 2(a) is marked as the coloured area in Fig. 27. It can be seen that the effective mass of the particle just becomes negative within the first band gap area. Hence, it is clearly confirmed that the first band gap is formed by the locally resonant mechanism.

Appendix II

Based on Eqs. and, the amplitude ratios of the eigenstates on the acoustic and optical bands are plotted out in Fig. 28, from which one can identify the characteristics of the eigenstates at the band-edge points.

Appendix III

Two conceptualized physical models of the proposed topological beam with deep subwavelength interface states are demonstrated in Fig. 29.

In the first conceptualized physical model shown in Fig. 29(a), the negative springs are realized using the preloaded three-spring devices [34]. In practical applications, a three-spring device exhibits a negative stiffness behaviour only over a small range of displacements, which is a limitation that needs to be considered. Fig. 29(b) presents another possible design. The negative springs are realized by using negative capacitor shunted piezoelectric elements [35]. In this design, a 'spring' connection is not realized at a

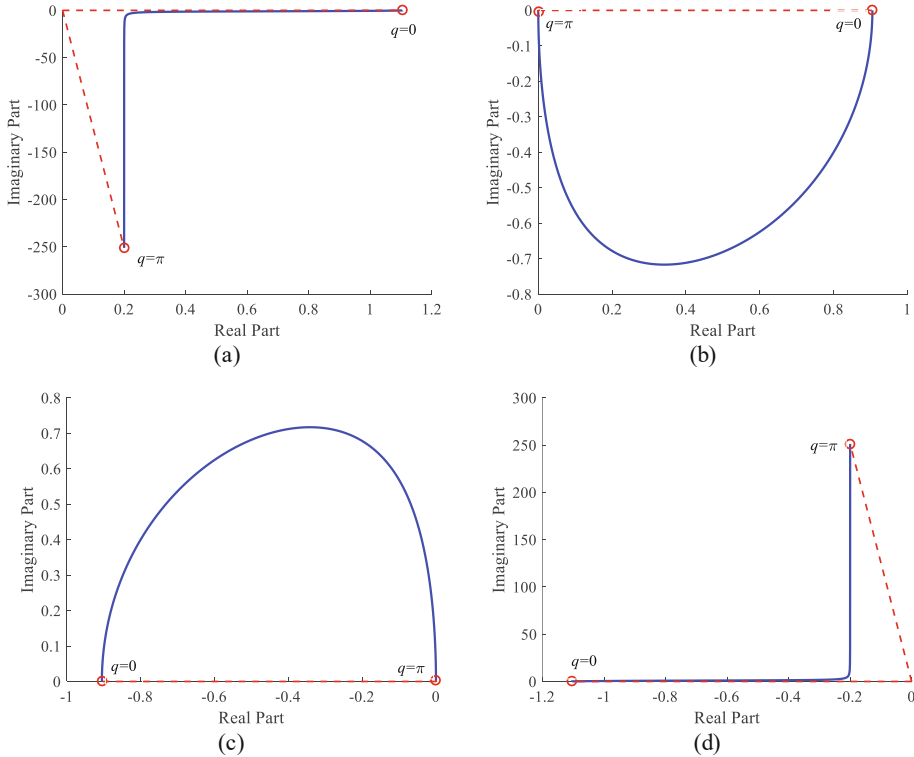


Fig. 28. Amplitude ratios of the eigenstates on the acoustic band: (a) $\alpha_1 = 0.1$ and $\alpha_2 = 0.5$, (b) $\alpha_1 = 0.5$ and $\alpha_2 = 0.1$; amplitude ratios of the eigenstates on the optical band: (c) $\alpha_1 = 0.1$ and $\alpha_2 = 0.5$, (d) $\alpha_1 = 0.5$ and $\alpha_2 = 0.1$. Note that in (a) and (d), when q approaches π , the imaginary part approaches infinity.

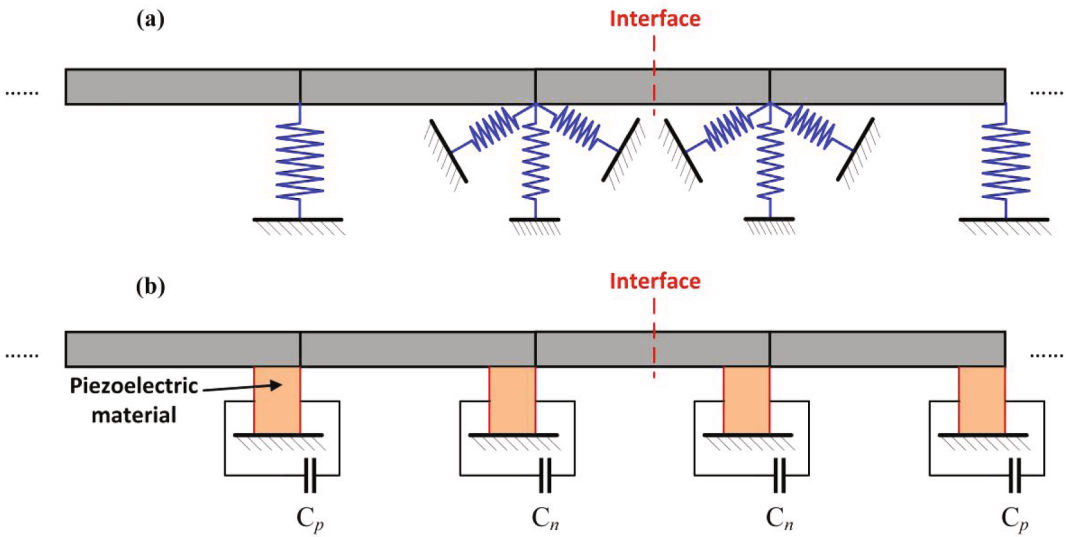


Fig. 29. Conceptualized physical models of the proposed topological beam with grounded springs realized using (a) pre-loaded three-springs devices; (b) negative capacitor shunted piezoelectric elements.

discrete point, but over a small portion of the beam. However, the equations presented in this paper are derived by assuming that a spring connection only acts at a discrete point on the beam. Hence, modifications are needed to take account of this effect. Moreover, the governing equation of the ‘spring’ constraint also need to be modified, since the ‘spring’ is realized by a continuous element rather than an ideal lumped element.

Appendix IV

Fig. 30(a) and **(b)** graphically illustrate the two types of base excitation conditions. It can be seen that under the excitation condition illustrated in **Fig. 30(a)**, the base excitation comes only from the left-hand side of the supercell beam lattice. However, for the excitation condition shown in **Fig. 30(b)**, the springs connected to the ground are also subjected to the same base excitation, and the ground is regarded as a general base.

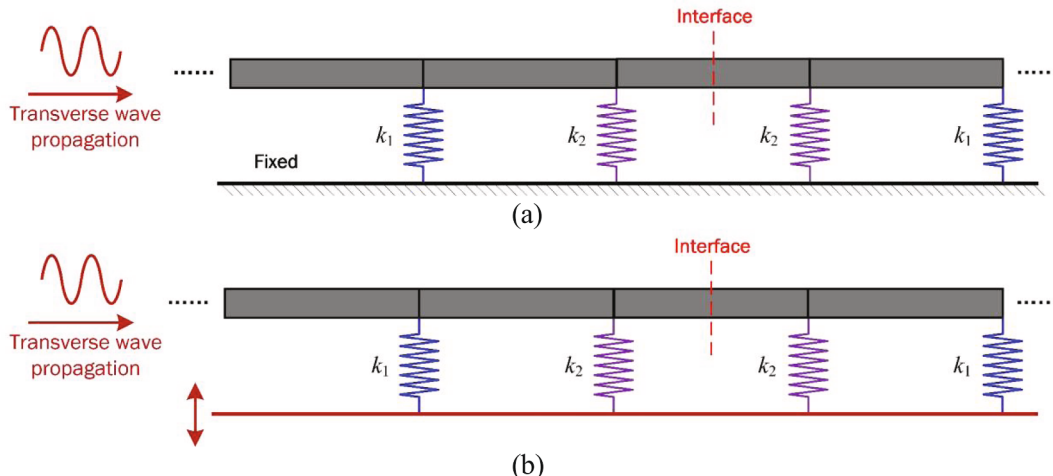


Fig. 30. (a) The base excitation is input from the left-hand side of the supercell beam lattice. The springs are connected to the ground at the absolutely static status. (b) The base excitation is regarded as the ground movement, i.e., the ground is deemed as a general base. In addition to the base excitation coming from the left-hand side of the supercell beam lattice, the springs connected to the ground are also subjected to the same base excitation.

References

- [1] J.E. Moore, The birth of topological insulators, *Nature* 464 (7286) (2010) 194–198.
- [2] S. Sasaki, M. Kriener, K. Segawa, K. Yada, Y. Tanaka, M. Sato, Y. Ando, Topological superconductivity in Cu x Bi 2 Se 3, *Physical review letters* 107 (21) (2011), 217001.
- [3] Schindler, F., A.M. Cook, M.G. Vergniory, Z. Wang, S.S. Parkin, B.A. Bernevig, and T. Neupert, *Higher-order topological insulators*. Science advances, 2018. 4(6): p. eaat0346.
- [4] A. Foehr, O.R. Bilal, S.D. Huber, C. Daraio, Spiral-based phononic plates: From wave beaming to topological insulators, *Physical review letters* 120 (20) (2018), 205501.
- [5] L.i. Xin, Y.u. Siyuan, L. Harry, L.u. Minghui, C. Yanfeng, Topological mechanical metamaterials: A brief review, *Current Opinion in Solid State and Materials Science* 24 (5) (2020) 100853, <https://doi.org/10.1016/j.cossms.2020.100853>.
- [6] A. Ghatak, M. Brandenbourger, J. van Wezel, C. Coulais, Observation of non-Hermitian topology and its bulk-edge correspondence in an active mechanical metamaterial, *Proceedings of the National Academy of Sciences* 117 (47) (2020) 29561–29568.
- [7] H. Fan, B. Xia, L. Tong, S. Zheng, D. Yu, Elastic higher-order topological insulator with topologically protected corner states, *Physical review letters* 122 (20) (2019), 204301.
- [8] S.H. Mousavi, A.B. Khanikaev, Z. Wang, Topologically protected elastic waves in phononic metamaterials, *Nature communications* 6 (1) (2015) 1–7.
- [9] D.J. Apigo, W. Cheng, K.F. Dobiszewski, E. Prodan, C. Prodan, Observation of topological edge modes in a quasiperiodic acoustic waveguide, *Physical review letters* 122 (9) (2019), 095501.
- [10] G. Ma, M. Xiao, C.T. Chan, Topological phases in acoustic and mechanical systems, *Nature Reviews Physics* 1 (4) (2019) 281–294.
- [11] R. Stöckl, S.D. Huber, Observation of phononic helical edge states in a mechanical topological insulator, *Science* 349 (6243) (2015) 47–50.
- [12] J. Zheng, Z. Luo, C. Jiang, J. Gao, Robust topology optimization for concurrent design of dynamic structures under hybrid uncertainties, *Mechanical Systems and Signal Processing* 120 (2019) 540–559.
- [13] L. Sirota, D. Sabovich, Y. Lahini, R. Ilan, Y. Shokef, Real-time steering of curved sound beams in a feedback-based topological acoustic metamaterial, *Mechanical Systems and Signal Processing* 153 (2021), 107479.
- [14] C. Lan, G. Hu, L. Tang, Y. Yang, Energy localization and topological protection of a locally resonant topological metamaterial for robust vibration energy harvesting, *Journal of Applied Physics* 129 (18) (2021) 184502, <https://doi.org/10.1063/5.0047965>.
- [15] Z. Wen, Y. Jin, P. Gao, X. Zhuang, T. Rabczuk, B. Djafari-Rouhani, Topological cavities in phononic plates for robust energy harvesting, *Mechanical Systems and Signal Processing* 162 (2022), 108047.
- [16] W.P. Su, J.R. Schrieffer, A.J. Heeger, Solitons in polyacetylene, *Physical review letters* 42 (25) (1979) 1698–1701.
- [17] Z. Yang, B. Zhang, Acoustic type-II Weyl nodes from stacking dimerized chains, *Physical review letters* 117 (22) (2016), 224301.
- [18] M. Xiao, G. Ma, Z. Yang, P. Sheng, Z.Q. Zhang, C.T. Chan, Geometric phase and band inversion in periodic acoustic systems, *Nature Physics* 11 (3) (2015) 240–244.
- [19] R.K. Pal, M. Ruzzene, Edge waves in plates with resonators: an elastic analogue of the quantum valley Hall effect, *New Journal of Physics* 19 (2) (2017) 025001, <https://doi.org/10.1088/1367-2630/aa56a2>.
- [20] Muhammad, W. Zhou, C.W. Lim, Topological edge modeling and localization of protected interface modes in 1D phononic crystals for longitudinal and bending elastic waves, *International Journal of Mechanical Sciences* 159 (2019) 359–372.
- [21] J. Yin, M. Ruzzene, J. Wen, D. Yu, L. Cai, L. Yue, Band transition and topological interface modes in 1D elastic phononic crystals, *Scientific reports* 8 (1) (2018) 1–10.
- [22] D. Zhao, M. Xiao, C.W. Ling, C.T. Chan, K.H. Fung, Topological interface modes in local resonant acoustic systems, *Physical Review B* 98 (1) (2018), 014110.

- [23] L. Fan, Y.e. He, X. Zhao, X.-a. Chen, Subwavelength and broadband tunable topological interface state for flexural wave in one-dimensional locally resonant phononic crystal, *Journal of Applied Physics* 127 (23) (2020) 235106, <https://doi.org/10.1063/5.0001548>.
- [24] S.H. Lee, C.M. Park, Y.M. Seo, Z.G. Wang, C.K. Kim, Acoustic metamaterial with negative modulus, *Journal of Physics: Condensed Matter* 21 (17) (2009) 175704, <https://doi.org/10.1088/0953-8984/21/17/175704>.
- [25] J.H. Oh, B. Assouar, Quasi-static stop band with flexural metamaterial having zero rotational stiffness, *Scientific Reports* 6 (2016) 33410.
- [26] G. Hu, L. Tang, J. Xu, C. Lan, R. Das, Metamaterial with Local Resonators Coupled by Negative Stiffness Springs for Enhanced Vibration Suppression, *Journal of Applied Mechanics* 86 (8) (2019), 081009.
- [27] D. Yu, J. Wen, H. Shen, Y. Xiao, X. Wen, Propagation of flexural wave in periodic beam on elastic foundations, *Physics Letters A* 376 (4) (2012) 626–630.
- [28] Y. Jin, W. Wang, B. Djafari-Rouhani, Asymmetric topological state in an elastic beam based on symmetry principle, *International Journal of Mechanical Sciences* 186 (2020), 105897.
- [29] W. Wang, Y. Jin, W. Wang, B. Bonello, B. Djafari-Rouhani, R. Fleury, Robust Fano resonance in a topological mechanical beam, *Physical Review B* 101 (2) (2020), 024101.
- [30] W.J. Drugan, Wave propagation in elastic and damped structures with stabilized negative-stiffness components, *Journal of the Mechanics and Physics of Solids* 106 (2017) 34–45.
- [31] A.A. Sarlis, D.T.R. Pasala, M.C. Constantinou, A.M. Reinhorn, S. Nagarajaiah, D.P. Taylor, Negative stiffness device for seismic protection of structures, *Journal of Structural Engineering* 139 (7) (2013) 1124–1133.
- [32] B.A. Fulcher, D.W. Shahan, M.R. Haberman, C. Conner Seepersad, P.S. Wilson, Analytical and experimental investigation of buckled beams as negative stiffness elements for passive vibration and shock isolation systems, *Journal of Vibration and Acoustics* 136 (3) (2014).
- [33] Y. Liu, D. Yu, L.i. Li, H. Zhao, J. Wen, X. Wen, Design guidelines for flexural wave attenuation of slender beams with local resonators, *Physics Letters A* 362 (5-6) (2007) 344–347.
- [34] H. Li, Y. Li, J. Li, Negative stiffness devices for vibration isolation applications: A review, *Advances in Structural Engineering* 23 (8) (2020) 1739–1755.
- [35] Y. Chen, G. Huang, C. Sun, Band gap control in an active elastic metamaterial with negative capacitance piezoelectric shunting, *Journal of Vibration and Acoustics* 136 (6) (2014).